

# A Self-Calibrating Halo-Based Group Finder: Application to SDSS

JEREMY L. TINKER<sup>1</sup>

<sup>1</sup>*Center for Cosmology and Particle Physics, Department of Physics, New York University, New York, USA, 10003*

Submitted to ApJ

## ABSTRACT

We apply a new galaxy group finder to the Main Galaxy Sample of the SDSS. This algorithm introduces new freedom to assign halos to galaxies that is self-calibrated by comparing the catalog to complementary data. These include galaxy clustering data and measurements of the total satellite luminosity from deep imaging data. We present constraints on the galaxy-halo connection for star-forming and quiescent populations. The results of the self-calibrated group catalog differ in several key ways from previous group catalogs and halo occupation analyses. The transition halo mass scale, where half of halos contain quiescent central galaxies, is at  $M_h \sim 10^{12.4} h^{-1} M_\odot$ , significantly higher than other constraints. Additionally, the width of the transition from predominantly star-forming halos to quiescent halos occurs over a narrower range in halo mass. Quiescent central galaxies in low-mass halos are significantly more massive than star-forming centrals at the same halo mass, but this difference reverses above the transition halo mass. We find that the scatter in  $\log M_*$  at fixed  $M_h$  is  $\sim 0.2$  dex for massive halos, in agreement with previous estimates, but rises sharply at lower halo masses. The halo masses assigned by the group catalog are in good agreement with weak lensing estimates for star-forming and quiescent central galaxies. We discuss possible improvements to the algorithm made clear by this first application to data. The group catalog is made publicly available.

*Keywords:* galaxies—groups: galaxies—halos

## 1. INTRODUCTION

One of the most striking features of the low-redshift galaxy population is the bimodality of galaxy properties. Galaxies can generally be categorized by their observed properties into two populations: the blue cloud and the red sequence (e.g., Baldry et al. 2004, 2006; Balogh et al. 2004; Blanton & Moustakas 2009). Blue cloud galaxies are actively star-forming, yielding blue colors and younger stellar populations as probed by their 4000-Å break (Kauffmann et al. 2003; Brinchmann et al. 2004). Red sequence galaxies have little to no star formation, resulting in red colors and large 4000-Å breaks in their spectra. Additionally, morphological properties correlate with these classifications: at fixed stellar mass, red galaxies are smaller, more concentrated, thus have higher velocity dispersions and stellar surface mass densities (Kauffmann et al. 2003; Blanton et al. 2003; Blanton & Moustakas 2009). Galaxy light profiles, quantified by Sersic-index  $n$ , exhibit a unimodal distribution, but the fraction of galaxies on the red se-

quence increases monotonically with Sersic- $n$  (Blanton et al. 2003). The fraction of galaxies within each mode of the color distribution is highly dependent on the large-scale environment around the galaxy (e.g., Baldry et al. 2004).

There is another galaxy property—though not an observable quantity—that has a strong influence on this bimodality: whether or not a galaxy is the central galaxy within its dark matter halo, or a satellite galaxy orbiting within the gravitational potential of a larger host halo. Galaxy group finders have been the most effective tool for quantifying the impact of the central-satellite dichotomy on the characteristics of the galaxy population (see, e.g., Weinmann et al. 2006; Blanton & Berlind 2007; Yang et al. 2008a, 2009; Peng et al. 2012; Wetzel et al. 2012, 2013; Tinker et al. 2017a). Among other results, these studies have demonstrated that correlations between galaxy properties and environment can be largely explained by simply separating galaxies into these two classes of halo occupation: central and satellite (Blanton & Berlind 2007; Peng et al. 2012; Tinker et al. 2017a, 2018; Tinker 2017).

These successes of galaxy group finders have also highlighted the need for improvements in algorithms used. Campbell et al. (2015) demonstrated that the halo

masses estimated for groups, especially when separating the central galaxies into star-forming and quiescent populations, can be significantly biased. In Paper I (Tinker 2020), we presented a new galaxy group finder, based on the halo-based algorithm of Yang et al. (2005), that ameliorates this issue, as well as improving on purity and completeness of central and satellite galaxy classifications when separating galaxies into their bimodal populations. The main advancement of the group finding algorithm in Paper I is to introduce new freedom into the model to account for possible unknown differences in galaxy-halo connection for star-forming and quiescent galaxies, and then self-calibrate these new degrees of freedom by comparing the predictions of the group catalog to various observational statistics, including galaxy two-point clustering and cross-correlations with faint imaging galaxies around spectroscopic central galaxies.

Understanding how the galaxy-halo connection differs for galaxies on opposite side of the bimodality is a key question in galaxy formation. What role does the dark sector play in building up the red sequence and making galaxies ‘red-and-dead?’ Unfortunately, different studies reach disparate conclusions. In a recent review, Wechsler & Tinker (2018) compiled observational constraints of the galaxy-halo connection for star-forming and quiescent galaxy population. The studies used halo occupation techniques to model galaxy mass functions, clustering, and (for some) galaxy-galaxy lensing, from the SDSS Main Galaxy Sample (MGS; York et al. 2000; Strauss et al. 2002). At a given halo mass,  $M_h$ , these models constrain the relative stellar masses,  $M_*$ , of star-forming and quiescent central galaxies. Some models predict quiescent galaxies are more massive, some predict that star-forming centrals are more massive, and others are consistent with the galaxies having the same stellar mass. Each of these scenarios have different implications for the relative importance of the dark halo in galaxy quenching, and which aspect of the dark halo—the halo mass or its formation history—is determinative.

Galaxy group catalogs can help resolve the discrepancy between various methods of quantifying the galaxy-halo connection. Unfortunately, they require datasets that are both large-volume and highly complete, both in terms of their target selection and in terms of redshift completeness. In the near future, such datasets will be expanded by large factors. The Bright Galaxy Survey of the Dark Energy Spectroscopic Instrument survey (DESI-BGS; DESI Collaboration et al. 2016), will produce an MGS-like sample of galaxies but larger by nearly a factor of 20 both in terms of volume and number of spectra. The WAVES project (Driver et al. 2016) will produce both wide and deep surveys that will be complementary to the BGS sample. The MGS is an ideal testbed for developing the next generation of galaxy group finders in advance of upcoming data. The goal of this paper is both to understand the galaxy-halo

connection in the local universe, but also to assess the efficacy of the self-calibrated algorithm with a representative data sample.

This paper is organized as follows: in §2 we present the data utilized, including the measurements incorporated into the self-calibration process. In §3, we review the self-calibrated group-finding algorithm presented in Paper I, including enhancements for analyzing the full MGS sample. In §4 we present our results. The results will focus on the galaxy-halo connections for our definitions of star-forming and quiescent, but in this section we will also compare to results from myriad previous studies. In §5 we discuss the results, both in terms of galaxy formation and in terms of assessing the current algorithm and identifying aspects that require improvement. As with Paper I, our results are based in part on the Bolshoi-Planck simulation (Klypin et al. 2016). For distance-redshift calculations, as well as theoretical calculations of the halo statistics, we use the same cosmology as in that simulation:  $(\Omega_m, \sigma_8, \Omega_b, n, h) = (0.307, 0.82, 0.048, 0.96, 0.7)$ . In this work, we define dark matter halos as having a mean interior density 200 times the background density. We also define halos as being distinct—i.e., they do not exist within the radii of a larger halo.

## 2. DATA

The data we use come from two main sources: SDSS MGS, and the DESI Legacy Imaging Surveys (DLIS; Dey et al. 2019). For the MGS, we use `dr72bright34` sample from the NYU Value-Added Galaxy Catalog (Blanton et al. 2005), which includes a total sample of 559,028 spectroscopic galaxies<sup>1</sup>. Derived properties, specifically the galaxy stellar masses,  $M_*$ , and 4000-Å breaks,  $D_n4000$ , come from the MPA-JHU reductions, which are available with the SDSS DR8 public data release and described in Brinchmann et al. (2004). Although the group-finding process is based on luminosity, we will examine the catalog results as a function of stellar mass as well. Our fiducial stellar masses are the PCA-based stellar masses of Chen et al. (2012), which were used in Alpaslan & Tinker (2020).

For all  $L_{\text{sat}}$  measurements, we use DLIS DR6 and DR7. DR6 represents northern imaging,  $\text{Dec} > 30^\circ$ , from the Mayall and Bok telescopes (Zhou et al. 2018), while the area below that declination is imaged by DECam (Flaugher et al. 2015). Together, these data cover roughly 75% of the SDSS footprint. The  $L_{\text{sat}}$  measurements used in this analysis are presented in Tinker et al. (2019a) and Alpaslan & Tinker (2020).

<sup>1</sup> This includes the  $\sim 7\%$  of galaxies that did not have a fiber assigned to them because of fiber collisions. We use the nearest-neighbor redshift assignment within the VAGC sample for distance and redshift. For properties derived from the spectroscopy, such as  $D_n4000$ , we assign each collided galaxy the properties of its nearest neighbor within color-magnitude space.

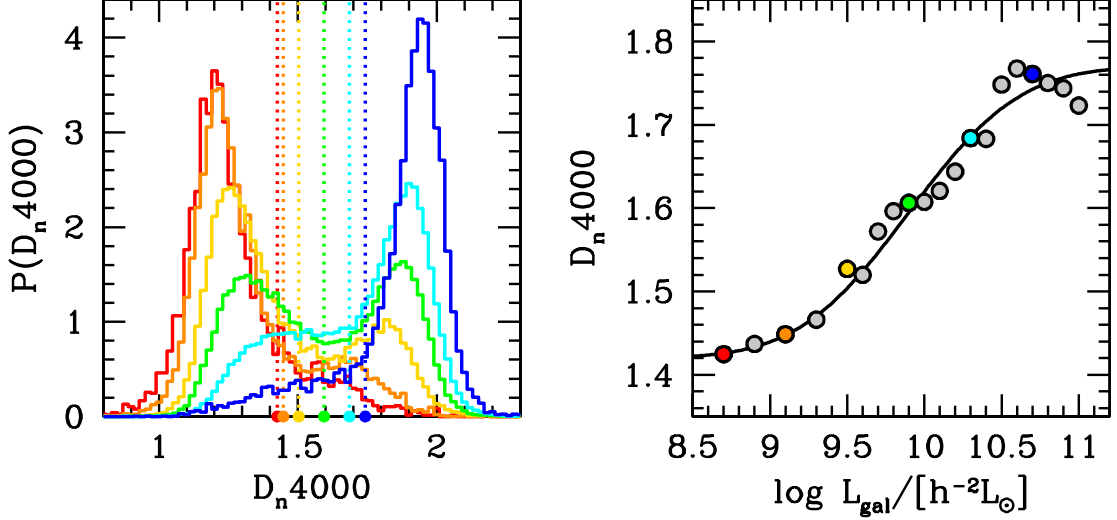


**Figure 1.** *Left Panel:* Distributions of  $D_{n4000}$  in 6 different bins of galaxy luminosity. The colors of each histogram correspond to the colored points in the right-hand panel, which indicates the value of  $L_{\text{gal}}$  for each bin. The vertical dotted line ending in the filled circle on the  $x$ -axis is the break-point between the star-forming and quiescent populations derived from the Gaussian Mixture Modeling analysis described in the text. *Right Panel:* The values of  $D_{n4000}$  where the two Gaussians in the GMM modeling have the same value, which we use as the population break point. The individual points represent the GMM results in each  $L_{\text{gal}}$  bin, while the smooth curve is the fitting function used in the analysis. The vertical lines in the left-hand panel correspond to the values from the fitting function.

### 2.1. Defining Quiescent and Star-Forming Samples

In order to separate galaxies into quiescent and star-forming samples, we must first define the break-point between these two classifications. A number of definitions have been used across the field: a single broadband color, color-color diagrams, star formation rates, emission line equivalent widths, and  $D_{n4000}$ . Additionally, the division between star-forming and quiescent can be a constant, or a function of galaxy luminosity or stellar mass.

In this paper, we use  $D_{n4000}$  to separate the two populations of galaxies. This quantity is significantly less sensitive to dust than broadband colors, and any aperture bias is minimal—for galaxies below the knee in the luminosity function, up to a quarter of those classified as red by the  $g-r$  color criterion are star-forming galaxies reddened by dust (Zhu et al. 2011).  $D_{n4000}$  identifies a significant fraction of low-luminosity galaxies that are classified as red by dust attenuation, but are intrinsically star-forming (Tinker et al. 2011). Although the fiber aperture of SDSS spectra only subtends the central part of the galaxy, misidentifying a blue galaxy as quiescent through  $D_{n4000}$  is relatively rare, and usually occurs for very low redshift objects (Geha et al. 2012).

It is convenient to set the threshold between star-forming and quiescent samples as a constant value of  $D_{n4000}$  or  $g-r$ , but the red sequence has a ‘tilt,’ such that brighter quiescent objects have redder colors and larger  $D_{n4000}$  values. This has motivated many studies to have dividing lines that vary with galaxy mass or luminosity (e.g., Li et al. 2006; Zehavi et al. 2011)

To account for this, we use Gaussian-mixture modeling (GMM) to determine the two populations as a function of  $L_{\text{gal}}$ . Figure 1 shows the distribution of  $D_{n4000}$  for multiple bins in  $\log L_{\text{gal}}$ . In each bin, we fit a two-Gaussian model to the distribution. We set the  $D_{n4000}$  value at which the two Gaussians cross as the threshold separating star-forming and quiescent populations. The vertical lines in this panel show this threshold value.

The right-hand panel in Figure 1 shows the results of the GMM in each  $L_{\text{gal}}$  bin. The solid curve represents a fit to these results, of the form

$$D_{\text{crit}} = 1.42 + \frac{0.35}{2} \left[ 1 + \text{erf} \left( \frac{\log L_{\text{gal}} - 9.9}{0.8} \right) \right], \quad (1)$$

where erf is the error function. We use Eq. (1) to separate star-forming and quiescent galaxy samples.

What impact do these choices on the quiescent fractions of galaxies? For the purposes determining the LHMR of galaxies, it is the quiescent fraction of central galaxies that is most important. The relative numbers of star-forming and quiescent galaxies are a factor in determining the halo masses, since each halo must have one central galaxy. Figure 2 compares  $f_q$  for multiple definitions of quiescence found in the literature. The sample of galaxies is taken from the volume-limited group catalog for  $M_r - 5 \log h < -18$  using the standard halo-based group finder of Tinker et al. (2011). This figure is for comparative purposes only, but we note that reproducing this figure using the final results of this pa-

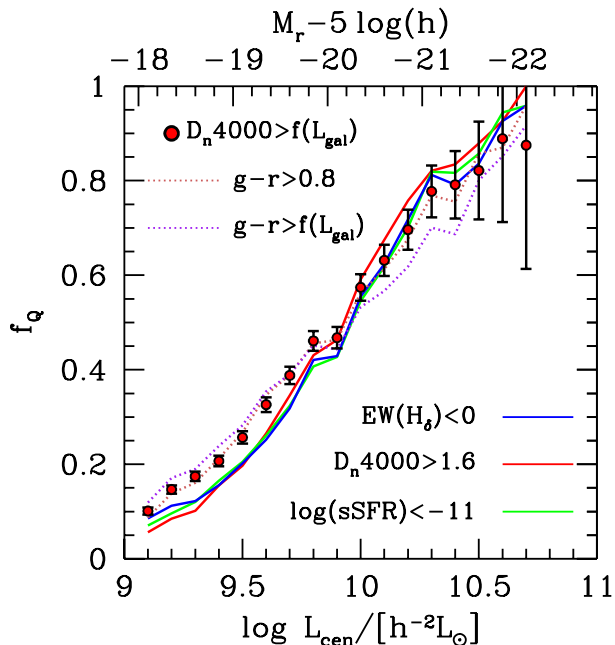


**Figure 2.** Comparison of the quiescent fraction of central galaxies for various definitions of quiescent in the literature. All results are applied to the volume-limited group catalogs of Tinker et al. (2011). The points with error bars represent the GMM split shown in Figure 1. The dotted lines indicate splits based on  $g - r$  colors; the purple dotted line is the ‘tilted’ cut from Zehavi et al. (2011) while the orange dotted curve represented the constant cut used in Mandelbaum et al. (2016). The solid curves show splits based on spectroscopic quantities: the equivalent width of the  $H_\delta$  emission line, the 4000-Angstrom break, and the specific star-formation rate, sSFR.

per yield negligible results in the differences between the definitions.

The GMM method of this paper is shown with the filled circles. Splits based on  $g - r$  color are indicated with dotted curves, while common methods based on spectroscopic quantities are shown with the solid curves. The two color-based cuts are taken from Mandelbaum et al. (2016) and Zehavi et al. (2011). The constant  $g - r > 0.8$  is utilized by the former, while the latter study uses the tilted threshold that varies linearly with  $M_r - 5 \log h$ . All of the results show qualitatively similar results, with the photometric splits yielding slightly higher  $f_q$  at low luminosities. This is likely due to the presence of dust in the central galaxies. Because the GMM results move the  $D_{\text{crit}}$  threshold lower for fainter galaxies, our GMM split is most comparable to the constant  $g - r$  threshold.

## 2.2. Projected Galaxy Clustering

Now that we have established the separation between star-forming and quiescent galaxies, we turn to measurements of their clustering. Figure 3 shows the projected

correlation function in four bins of magnitude. For each magnitude bin, we have constructed volume-limited samples within which to measure the clustering. Error bars are calculated using the jackknife technique, separating the distribution of galaxies and randoms into 25 roughly equal-area regions in the plane of the sky. The clustering results here are in agreement with previous measurements at low-redshift galaxy clustering, with the red galaxies having higher clustering amplitude at all scales and for all magnitudes.

Figure 3 also compares our measurements to those of Zehavi et al. (2011). Zehavi uses the DR7 SDSS MGS, as well as the same binning in magnitude. The only difference is the star-forming/quiescent threshold. Figure 2 demonstrated that the difference in central galaxies is minimal, and this is reflected in the clustering measurements.

## 2.3. Total Satellite Luminosity

As presented in Paper I, one of the key ingredients in the self-calibration method is the inclusion of measurements of total satellite luminosity,  $L_{\text{sat}}$ . A full explanation of the method is presented in Tinker et al. (2019b). In brief,  $L_{\text{sat}}$  measures the total amount of  $r$ -band luminosity around spectroscopic central galaxies using deep imaging data from the DLIS. Because there is no redshift information in the imaging galaxies,  $L_{\text{sat}}$  is measured by first stacking a set of central galaxies in a given bin and subtracting a background value of imaging galaxies. For all spectroscopic galaxies,  $L_{\text{sat}}$  is measured within fixed comoving apertures of  $50 h^{-1} \text{kpc}$ .

Paper I demonstrated that these data provide significant constraining power on the relative halo masses of star-forming and quiescent central galaxies at fixed  $L_{\text{cen}}$ . Using only the satellites available in the spectroscopic catalog is not sufficient to determine if these two subsamples of galaxies live in different halos at fixed luminosity.

Figure 4 shows the measurements of  $L_{\text{sat}}$  for star-forming and quiescent central galaxies that are incorporated into the self-calibrated group finder. The top panel shows the raw measurements of  $L_{\text{sat}}$  as a function of  $L_{\text{cen}}$ . The bottom panel shows the actually data that the group finder is fit to: the relative measurements at fixed  $L_{\text{cen}}$ ,  $L_{\text{sat}}^q / L_{\text{sat}}^{\text{sf}}$ . The reason behind using the relative values rather than the absolute values is that it reduces systematic errors, both in terms of the measurements and the theoretical modeling. Errors in the background subtraction, as well as miscalibrations between the Legacy Surveys imaging data and the SDSS imaging, which we use here to make our model predictions (which we describe in more detail in §3 and Paper I). Additionally, numerical resolution can impact the number of subhalos (van den Bosch & Ogiya 2018; van den Bosch et al. 2018). This can lower the predicated value of  $L_{\text{sat}}$  from a simulation, but the effects are reduced when calculating the ratio of satellite luminosities.



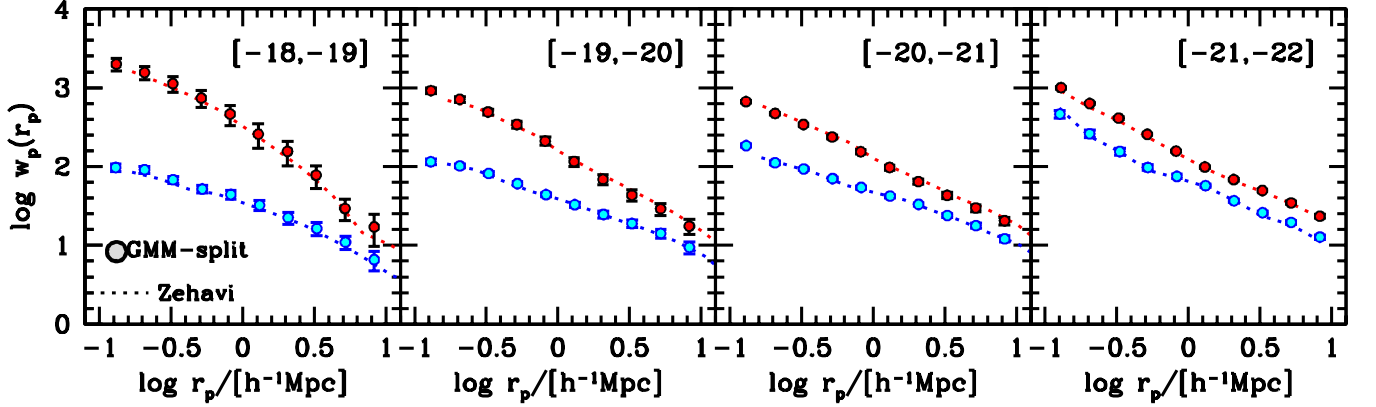


**Figure 3.** Projected correlation function in volume-limited samples within the full flux-limited MGS. The magnitude bin is indicated in the top right corner of each panel. Blue and red symbols indicate star-forming and quiescent galaxy samples, as constructed by the GMM analysis in Figure 1. These data are included in the self-calibration of the group finder. The dotted lines in the first three magnitude bins show the results from Zehavi et al. (2011). There is no measurement from Zehavi for the brightest bin, so in the  $[-21, -22]$  bin the dotted lines show the results with a constant  $D_n 4000 > 1.6$  split between star-forming and quiescence.

The bottom panel in Figure 4 shows the  $L_{\text{sat}}^q/L_{\text{sat}}^{\text{sf}}$  ratio. For bright central galaxies, quiescent central galaxies are halos with roughly twice the satellite luminosity (within the aperture). At lower luminosities, the data suggest that the ratio gets closer to unity, but the large error bars make prevent any conclusions from inspection of the measurements.

#### 2.4. Secondary Galaxy Properties

In addition to measuring  $L_{\text{sat}}$  as a function of luminosity, the key result from Alpaslan & Tinker (2020) is that most galaxy secondary properties also carry information about their dark matter halos. At fixed galaxy stellar mass,  $L_{\text{sat}}$  correlates with properties such as stellar velocity dispersion, galaxy size, and morphological properties.

These correlations do not, by themselves, imply correlations between galaxy properties and  $M_h$ . Halo formation history also impacts the amount of subhalos within a host halo, thus correlating with the amount of satellite luminosity. To break this degeneracy, the test proposed by Tinker et al. (2019b) is to measure the correlation between the central galaxy secondary secondary property and the large-scale environment. If the correlation between  $L_{\text{sat}}$  and secondary property is due to a correlation between halo formation history and the property, the property will exhibit a correlation with the large-scale environment. This is due to the correlation between halo formation history and large-scale environment: older, more concentrated halos form in high density regions of the cosmic web.

To increase our ability to properly assign halo masses to central galaxies, we use galaxy concentration as the secondary parameter. Concentration,  $c_{\text{gal}}$ , is defined as the ratio between the radius that contains 90% of the

galaxy light to the half-light radius. There are several reasons behind this choice: (1)  $c_{\text{gal}}$  for central galaxies shows no correlation with large-scale environment at fixed stellar mass, (2)  $c_{\text{gal}}$  shows a correlation with  $L_{\text{sat}}$  that is roughly independent if  $M_*$  (Alpaslan & Tinker 2020), and (3)  $c_{\text{gal}}$  varies minimally with galaxy luminosity.

As in Paper I, we transform the secondary property into a normalized parameter,  $\chi \equiv (c_{\text{gal}} - \bar{c})/\sigma_c$ , where  $\bar{c}$  and  $\sigma_c$  are the mean and standard deviation of  $c_{\text{gal}}$  and are continuous functions of  $L_{\text{cen}}$ . Figure 5 shows  $\bar{c}$  and  $\sigma_c$  as a function of  $L_{\text{cen}}$  separately for star-forming and quiescent galaxies. The middle panels show the distributions of  $\chi$  for the two populations of central galaxies.

We take the measurements of  $L_{\text{sat}}$  for each galaxy and normalize it by the expected value of  $L_{\text{sat}}$  given the galaxy luminosity. This is given by the mean  $L_{\text{sat}} - L_{\text{cen}}$  relation, derived independently for star-forming and quiescent central galaxies. This removes the overall trend of  $L_{\text{sat}}$  with luminosity, leaving only the residuals of  $L_{\text{sat}}$  as a function of  $\chi$ . Galaxies are binned by  $\chi$  and in each bin the mean value is calculated;

$$\tilde{L}_{\text{sat}}(\chi) = \frac{1}{N} \sum_i \frac{L_{\text{sat},i}}{L_{\text{sat}}(L_{\text{cen},i})}, \quad (2)$$

where  $N$  is the number of galaxies in the bin of  $\chi$ , and  $i$  is the index of all galaxies within the bin of  $\chi$ .

The results for both star-forming and quiescent subsamples in the right-hand column of Figure 5. As expected from the Alpaslan & Tinker (2020) results, both of these galaxy subsamples show significant correlations between  $\chi$  and  $L_{\text{sat}}$ . But here the measurement has significantly higher signal-to-noise given that all galaxies are combined into a single measurement. For star-forming galaxies,  $L_{\text{sat}}$  is positively correlated with  $\chi$ ,

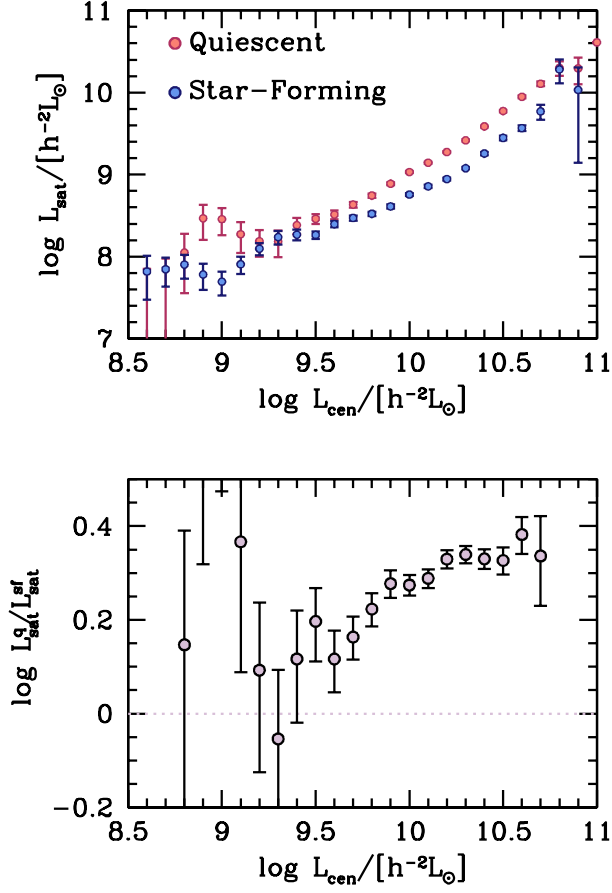


**Figure 4.** *Top Panel:*  $L_{\text{sat}}$  as a function of  $L_{\text{cen}}$  for star-forming and quiescent subsamples of galaxies. Error bars are from the bootstrap method, sampling from the population of central galaxies. *Bottom Panel:*  $L_{\text{sat}}$  ratio between quiescent and star-forming galaxies at fixed  $L_{\text{cen}}$ . These data are the ones included in the self-calibration of the group finder.

meaning higher-concentrated galaxies live in halos with more satellite luminosity, most likely due to higher halo masses. The values of  $L_{\text{sat}}$  vary by nearly 0.6 dex, or a factor of four. The correlation for quiescent galaxies is even more extreme: varying by nearly 0.8 dex in a smaller range of  $\chi$ , from -1 to +1. Outside of this range, the trends plateau at their maximum and minimum values.

### 3. METHODS

A full outline of the self-calibration method is presented in Paper I. Here we briefly review the algorithm, introducing the variables that will be fit in the self-calibration process.

#### 3.1. Free parameters in the model

The halo-based group finder uses an initial estimate of the halo mass around a central galaxy to determine

the probability that neighboring galaxies are satellites within the halo. Then the halo mass is re-estimated by a rank-ordering of the halos by their total luminosity, which is abundance-matched onto the halo mass function. A neighbor is considered a satellite if  $P_{\text{sat}} > 0.5$ , where

$$P_{\text{sat}} = \left[ 1 - (1 + P_{\text{proj}} P_z / B_{\text{sat}})^{-1} \right], \quad (3)$$

where  $P_{\text{proj}}$  and  $P_z$  are the projected and line-of-sight probabilities, respectively.  $B_{\text{sat}}$  is a free parameter setting the threshold probability. In the standard group-finder,  $B_{\text{sat}} = 10$  independent of galaxy type or luminosity. In the self-calibrated algorithm,  $B_{\text{sat}}$  is a function of  $L_{\text{gal}}$ , parameterized as

$$B_{\text{sat},c} = \beta_{0,c} + \beta_{L,c} (\log L_{\text{gal}} - 9.5), \quad (4)$$

where the class of the galaxy is indicated by  $c = sf$  or  $q$  for star-forming and quiescent galaxies, respectively.  $B_{\text{sat}}$  cannot be negative, thus we implement a minimum value of  $B_{\text{sat}}$  of 0.01 when implementing the group finder.

Once all galaxies have been assigned to groups, halo masses are assigned to each group using abundance matching. In the standard implementation of the halo-based group finder, the total luminosity,  $L_{\text{tot}}$ , (or total stellar mass,  $M_{\text{tot}}$ ) of the group is abundance matched onto the theoretical estimate of the host halo mass function. In the self-calibrated model, we allow weight factors to be placed on a group given certain properties of the group.

First, we put separate weight factors on groups with star-forming and quiescent central galaxies. These weight factors are functions of  $L_{\text{cen}}$ , such that

$$\log w_{\text{cen},c} = \frac{\omega_{0,c}}{2} \left[ 1 + \text{erf} \left( \frac{\log L_{\text{gal}} - \omega_{L,c}}{\sigma_{\omega,c}} \right) \right], \quad (5)$$

where  $c$  indicates central galaxy class as in Eq. (4). Eq. (5) allows our two classes of galaxies to occupy different halos, even if the total group luminosity is the same.

To incorporate the information available in the  $\tilde{L}_{\text{sat}}(\chi)$  data, we introduce weights based on a central galaxy's  $\chi$  value, with

$$w_{\chi,c} = \exp \left[ \frac{\chi}{\omega_{\chi,c,0} + \omega_{\chi,c,L} (\log L_{\text{gal}} - 9.5)} \right], \quad (6)$$

where the exponential form is motivated by the log-linear dependence of  $L_{\text{sat}}$  on most galaxy properties at fixed  $M_*$  (Alpaslan & Tinker 2020), as well as the results of  $\tilde{L}_{\text{sat}}(\chi)$  in Figure 5. Eq. (6) introduces two new free parameters over the model in Paper I, in which the  $w_\chi$  weights were independent of  $L_{\text{gal}}$ . This was sufficient in the tests presented in Paper I because the mock

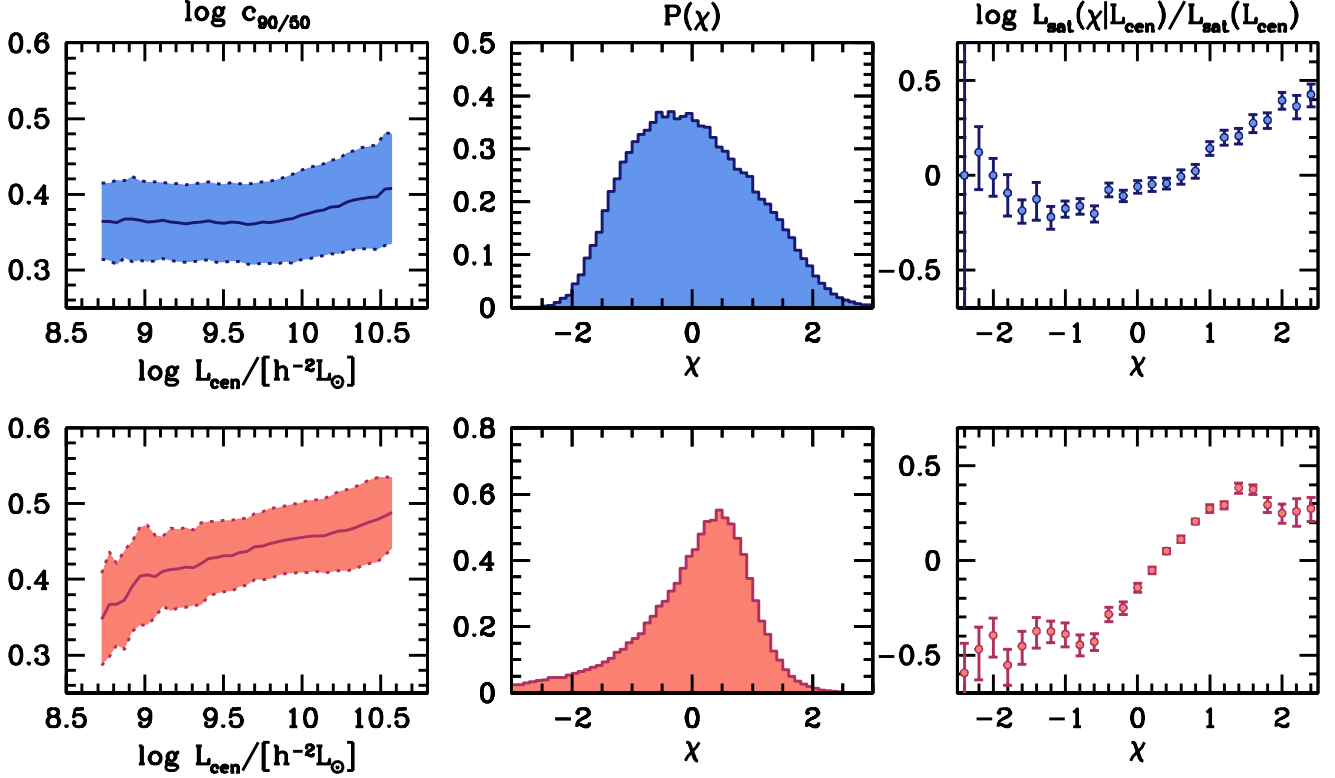


**Figure 5.** Incorporating the dependence of  $L_{\text{sat}}$  on galaxy concentration,  $c_{\text{gal}}$ , into the self-calibration method. The top row shows results for star-forming central galaxies, while the bottom row shows the results for quiescent central galaxies. *Left Column:* The correlation between  $\log c_{\text{gal}}$  and  $L_{\text{cen}}$ . The solid curve shows the mean value, while the shaded region shows the  $1\text{-}\sigma$  range of values. *Middle Column:* The distribution of  $\chi$ , defined as  $(c - \bar{c})/\sigma_c$ , where  $\bar{c}$  is taken from the solid curve the left column, and  $\sigma_c$  is the shaded region from those panels. *Right Column:* Correlation between  $L_{\text{sat}}$  and  $\chi$ . Here,  $L_{\text{sat}}$  for each galaxy is normalized by the mean value of  $L_{\text{sat}}$  at that value of  $L_{\text{cen}}$  for the given subsample. These data are incorporated into the self-calibration of the group finder.

galaxy distributions were constructed with correlations between  $\chi$  and  $M_h$  that were also independent of  $L_{\text{gal}}$ . In fitting the SDSS data, we find statistically improves results with this additional freedom.

This makes 14 total free parameters. These parameters are listed in Table 1. We also list the 68% confidence intervals resulting from the fitting procedure we describe in §3.3.

When rank-ordering groups, we use the weighted total luminosity,  $L_{\text{grp}} = L_{\text{tot}} \times w_{\text{cen},c} \times w_{\chi,c}$ . We define  $L_{\text{tot}}$  as the total  $r$ -band luminosity of spectroscopic galaxies within the group. This marks another minor change from Paper I, in which the weight factors were only applied to the central galaxy luminosity. Although the central galaxy dominates to group luminosity for the vast majority of groups, we find that the change yields an improved fit to the SDSS data.

### 3.2. Adaptation for flux-limited samples

Paper I demonstrated that the group finder efficiently identifies groups in volume-limited samples. Thus, when applying the algorithm to the flux-limited MGS sample, we treat the full sample as a series of smaller-volume

samples, each of which is much closer to a volume-limited sample than the full sample.

Each sub-volume has a redshift thickness of 0.05. Within each sub-volume, all galaxies above the flux limit are included. Thus, to account for the change in the magnitude limit across the redshift width of the bin, we use  $1/V_{\text{max}}$  weighting to calculate the number density of groups, based on the  $V_{\text{max}}$  value of the central galaxy. If  $V_{\text{max}}$  is larger than the volume of the of the upper redshift limit of the bin,  $V_{\text{max}}$  is set to be that volume of the upper limit. Thus, for the majority of groups in each redshift bin,  $V_{\text{max}}$  is equal to the volume of the bin itself.

To avoid discontinuities in how halos are assigned to galaxies, the redshift bins are finely spaced by only  $\Delta z = 0.005$ , and allowed to overlap. Thus a given group contributes to the number density in 10 bins. When assigning halo mass to a given group, we use the number density in the bin that is closest to the redshift of group's central galaxy. The abundance-matching expression used to convert weighted group luminosity to halo mass is

$$\sum_{L=L_{\text{grp}}}^{\infty} \frac{1}{V_{\text{max}}} = \int_{M_h}^{\infty} n_h(M'_h) dM'_h, \quad (7)$$

where  $n_h$  is the halo mass function (Tinker et al. 2008), and  $V_{\text{max}}$  is constrained by the redshift bin to which Eq. (7) is applied, as discussed above.

### 3.3. Outline of the method

To find the optimal set of parameters, we compare predictions from the group catalog to our observational quantities. In order to make these predictions, we use the group catalog produced by a given set of parameters to populate halos in an N-body simulation. For this analysis we use the Bolshoi Planck simulation (Klypin et al. 2016).

The procedure for implementing the self-calibrated group finder is as follows:

- Start with a set of values for the 14 free parameters of the model.
- Run the group finder with this set of parameters, iterating until the satellite fraction converges. This assigns  $M_h$  to each group and classifies every galaxy as central or satellite.
- Measure the halo occupation distribution (HOD; see Wechsler & Tinker 2018) within the resulting group catalog for each volume-limited bin for which  $w_p(r_p)$  is measured in the SDSS data.
- Populate the host halos of the Bolshoi-Planck N-body simulation with the HODs for each magnitude bin and measure the predicted clustering.
- Calculate the predicted value of  $L_{\text{sat}}^q/L_{\text{sat}}^{\text{sf}}$  for the group catalog using tabulated values for  $L_{\text{sat}}$  as a function of  $M_h$ .
- Calculate the predicted value of  $\tilde{L}_{\text{sat}}(\chi)$  for the group catalog using the same tabulation of  $L_{\text{sat}}$  as a function of  $M_h$ .
- Calculate the  $\chi^2$  value for the model by comparing the group catalog predictions to the SDSS data.

Following the outline above, for a given model, the total  $\chi^2$  is

$$\chi_{\text{tot}}^2 = \sum_{\text{sf}, q} \sum_{i=1}^{N_{\text{bins}}} \chi_{w_p, i}^2 + \chi_{L_{\text{sf}}/L_q}^2 + \sum_{c=\text{sf}, q} \chi_{L_{\chi}, c}^2 \quad (8)$$

where the first term is the  $\chi^2$  from the clustering data, summing over the two subsamples and four magnitude bins, the second term is from the  $L_{\text{sat}}^q/L_{\text{sat}}^{\text{sf}}$  data, and the last term is the  $\tilde{L}_{\text{sat}}(\chi)$  data, summing over both subsamples. When calculating  $\chi$ , we add in quadrature the errors from the observational data with the sample variance expected from the Bolshoi Planck simulation volume, which is  $250 h^{-1} \text{Mpc}$  on a side.

To find the best-fitting model, we use Powell’s method to minimize  $\chi_{\text{tot}}^2$ . To find the confidence intervals on the parameters, and thus our constraints on the halo masses assigned to each central galaxy, we use `emcee`, a public implementation of the Markov Chain Monte Carlo method (Foreman-Mackey et al. 2013).

## 4. RESULTS

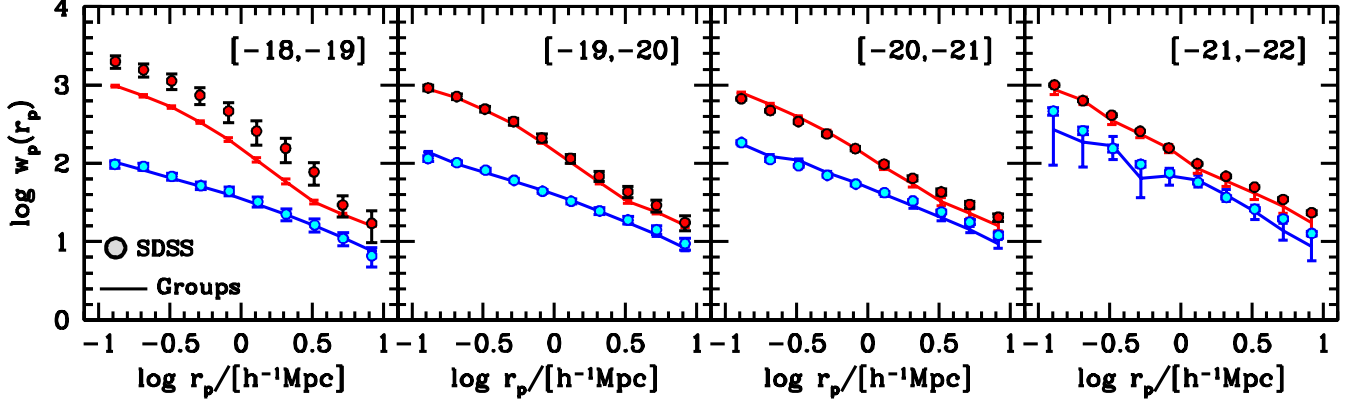
Here we present the results of the group finding process. We focus first on how well the group catalog can reproduce the measurements from SDSS, and the constraints they yield on the free parameters of the group finder. Next, we discuss the derived properties of the galaxy population. These include the satellite fractions of galaxies, the relations between halo mass and central galaxy properties—specifically luminosity and stellar mass, and the scatter between them. For many results, we will compare those derived from the fiducial self-calibrated group catalog to results in which the  $\tilde{L}_{\text{sat}}(\chi)$  data have been removed from the analysis, and all  $w_\chi$  weights are set to unity. We will refer to this catalog as ‘no- $\chi$ .’ The primary results will be referred to as the fiducial catalog. Where relevant, we will compare to complementary analyses from parametric halo occupation models and previous group finders.

### 4.1. Fits to the data

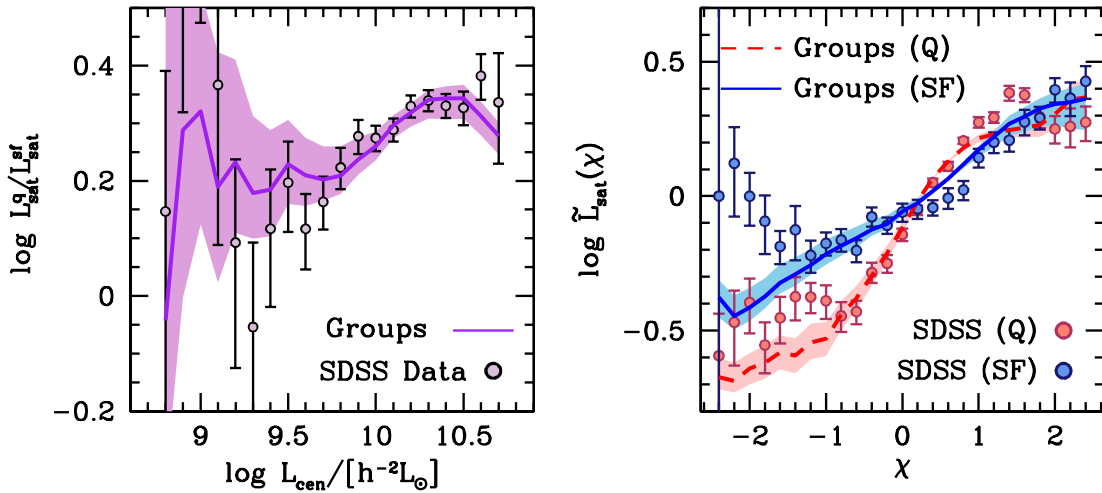
To recap, we have data from three different observed quantities: the projected correlation function,  $w_p(r_p)$ , the ratio of  $L_{\text{sat}}$  for star-forming and quiescent central galaxies, and the dependence of  $L_{\text{sat}}$  on central galaxy concentration, separated into measurements for star-forming and quiescent central galaxies. This yields a total data vector of 148 data points. The best-fit group catalog yields a  $\chi^2$  of 165. For 14 degrees of freedom, this value yields a  $P(>\chi^2)$  of 0.04. So while the model is a reasonable description of the data, the random chance of obtaining that  $\chi^2$  value is roughly a  $2\sigma$  deviation. The places where the fit can be improved in future iterations of the model are clear upon inspection of the fits themselves. We will discuss these subsequently.

Figure 6 shows the best-fit group catalog with the SDSS measurements of  $w_p(r_p)$ . At all luminosities and all scales, the group catalog yields enhanced clustering relative to star-forming galaxies. In most all magnitude bins, the group catalog fit is in excellent agreement with the data. However, the quiescent galaxies in the  $M_r - 5 \log h = [-18, -19]$  bin is clearly discrepant, significantly underpredicting the clustering amplitude.





**Figure 6.** Projected correlation functions yielded by the best-fit galaxy group catalog. Points with errors are the SDSS measurements from Figure 3. The solid curves are the best-fit model. Red points and curves indicate quiescent samples, while blue points and curves represent star-forming samples. The errors on the group catalog predictions are from the simulation volume, while the errors on each SDSS measurement are derived from sample sizes that increase with the magnitude limit. Thus, for the faint bin the observational error dominates, while for the brightest bin the theoretical error dominates.



**Figure 7.** *Left Panel:*  $L_{\text{sat}}^q/L_{\text{sat}}^{\text{sf}}$  yielded by the best-fit group catalog. Points with error bars are the  $L_{\text{sat}}$  SDSS measurements from Figure 4. The shaded region is the 95% confidence interval on this quantity. *Right Panel:*  $\tilde{L}_{\text{sat}}(\chi)$  produced by the best-fit group catalog. Points with error bars are the SDSS data from Figure 5. Red symbols and curve represent quiescent central galaxies, while blue symbols and curves represent star-forming central galaxies. Shaded regions around the curves are 95% confidence intervals.

Fort this one bin<sup>2</sup>, the extra freedom incorporated into the group finder is still not sufficient to match the data. We will discuss this in more detail in the next subsec-

tion., but this is the clearest place to improve the  $\chi^2$  of the model.

Figure 7 compares the group catalog to the different  $L_{\text{sat}}$  measurements. The left-hand panel presents  $L_{\text{sat}}^q/L_{\text{sat}}^{\text{sf}}$ , where the shaded region around the best-fit catalog is the 95% confidence interval on this quantity. The catalog yields a good fit to the data at all luminosities, but the constraints on the  $L_{\text{sat}}$  ratio widen significantly at low luminosities due to the large errors on this statistic. At the brightest luminosities, the turnover in the group catalog values is due to aperture for which  $L_{\text{sat}}$  is calculated. As halos get more massive, a smaller

<sup>2</sup> Although the fainter  $M_r - 5 \log h = [-17, -18]$  bin is not included in the fit, we note that the the group catalog also underpredicts the clustering amplitude of quiescent galaxies in this bin as well, while being in good agreement with the clustering of the star-forming sample. The error bars on this sample are too large for it's inclusion in the fit to have a significant effect on the best-fit model.

**Table 1.** Parameters of the Self-Calibrated Group Finder

Parameter	68% low	Median	68% high	Best fit
$\beta_{0,sf}$	11.79	13.52	15.17	12.49
$\beta_{L,sf}$	-10.38	-8.26	-6.59	-8.72
$\beta_{0,q}$	-1.22	-0.94	-0.69	-0.91
$\beta_{L,q}$	7.80	10.50	12.76	10.36
$\omega_{0,sf}$	13.34	17.64	22.97	16.84
$\omega_{L,sf}$	12.59	13.11	13.69	13.03
$\sigma_{\omega,sf}$	1.93	2.39	2.83	2.39
$\omega_{0,q}$	2.04	2.67	3.37	2.95
$\omega_{L,q}$	12.06	13.02	14.22	12.63
$\sigma_{\omega,q}$	3.70	4.87	6.28	4.20
$\omega_{\chi,sf,0}$	2.45	2.79	3.30	2.68
$\omega_{\chi,sf,L}$	1.75	2.18	2.58	2.34
$\omega_{\chi,q,0}$	1.03	1.12	1.23	1.11
$\omega_{\chi,q,L}$	0.31	0.47	0.57	0.43

NOTE—The first three numerical columns indicate the 68% confidence regions on each parameter from the MCMC analysis, as well as the median value of each parameter. The final column indicates the values of each parameter in the model that yields the lowest  $\chi^2$  value.

fraction of their area is subtended by the  $50 h^{-1}\text{kpc}$  aperture. Thus, although the total amount of satellites in a halo increases roughly linearly with host halo mass, the difference in  $L_{\text{sat}}$  between different halo masses gets smaller. From the shaded contours, it is clear that this turnover is statistically significant.

The right-hand panel in Figure 7 compares the model predictions to the measurements of  $\tilde{L}_{\text{sat}}(\chi)$  for star-forming and quiescent central galaxies. For the quiescent sample, the the model is able to fit both the steep slope in  $L_{\text{sat}}$  for galaxies within  $1\text{-}\sigma$  of the mean  $c_{\text{gal}}$ , as well as the plateaus in  $L_{\text{sat}}$  at the high and low values of  $\chi$ . For the star-forming galaxies, the models produce a monotonically increasing  $L_{\text{sat}}$  with  $\chi$ , which is in good agreement with the data at high  $\chi$ , but cannot fit the data at low  $\chi$ , where  $L_{\text{sat}}$  rises back up again.

Although the best-fit group catalog yields a reasonable description of the data, the largest discrepancies are with the clustering of faint red galaxies, the  $L_{\text{sat}}$  values of the most concentrated quiescent galaxies, and  $L_{\text{sat}}$  values of the least concentrated star-forming galaxies.

#### 4.2. Parameter constraints

The 68% confidence intervals on all the free parameters of the model, as well as the values of the best-fit

model, are listed in Table 1. Corner plots showing the posterior distributions of the parameters are shown in the Appendix.

Figure 8 shows the constraints on the three quantities that determine group membership and halo mass. The top panel shows the ratio of  $w_{\text{cen},q}$  to  $w_{\text{cen},sf}$  for groups. Although we parameterize these two quantities individually for maximal flexibility, the ratio is the quantity that matters for the rank-ordering of the groups themselves. At  $\log L_{\text{cen}} \lesssim 10.2$ , groups with quiescent central galaxies are down-weighted relative to groups with star-forming central galaxies. This means that, at fixed  $L_{\text{tot}}$ , quiescent-central groups receive lower halo masses. This reverses at higher central luminosities, where groups with star-forming centrals are de-weighted. This yields the fit to the  $L_{\text{sat}}^q/L_{\text{sat}}^{sf}$  data—at fixed  $L_{\text{cen}}$  (or  $L_{\text{tot}}$ ),  $L_{\text{sat}}^q$  is higher because these groups are assigned higher halo masses during rank-ordering. At lower masses, the range of  $L_{\text{sat}}$  ratios gets large due to weaker constraints on the weights and few quiescent central galaxies. The best-fit model, however, still yields  $L_{\text{sat}}^q > L_{\text{sat}}^{sf}$  due to the different scatters between the two samples, which we will discuss in §4.8.

The middle panel shows the constraints on  $B_{\text{sat}}$  for star-forming and quiescent galaxies. Recall that the standard implementation of the halo-based group finder

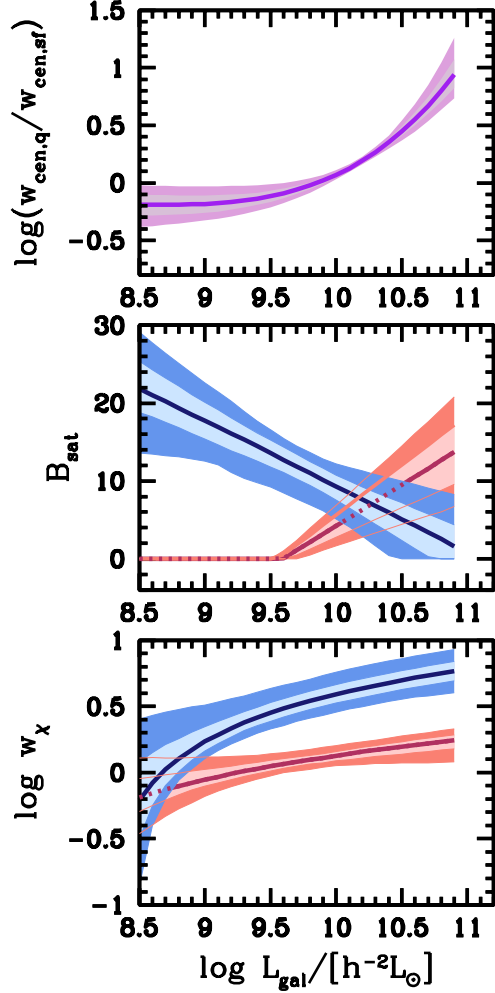


**Figure 8.** Constraints on the quantities that set the halo masses of groups and the membership probabilities of satellites. See §3.1 for all equations that utilize the parameters. *Top Panel:* Constraints on the ratio of  $w_{\text{red}}$  to  $w_{\text{blue}}$ . The solid curve is the best-fit group catalog, while the inner and outer shaded regions show the 68% and 95% value ranges. *Middle Panel:* Same as the top panel, but now for the satellite threshold value,  $B_{\text{sat}}$ . Blue and red contours represent results for the star-forming and quiescent galaxy samples, which are parameterized independently. *Bottom Panel:* Same as the middle panel, but here the contours represent the weights based on  $\chi$ , the normalized galaxy concentration parameter.

set  $B_{\text{sat}} = 10$ . For star-forming galaxies,  $B_{\text{sat}}$  decreases with increasing luminosity, being nearly twice as high as the standard value at the lowest luminosities considered. At the bright end,  $B_{\text{sat}}$  approaches zero.

For quiescent galaxies, the clustering requires that  $B_{\text{sat}}$  be at the lower limit of 0.01 for galaxies fainter than  $\log L_{\text{gal}} = 9.5$ .  $B_{\text{sat}}$  has a linear parameterization,

so for any combination of parameters that yield  $B_{\text{sat}}$  lower than the minimum value,  $B_{\text{sat}}$  is simply set to the minimum. Thus, large changes in the slope and intercept of  $B_{\text{sat}}$  may yield no differences in the actual value used for low-luminosity quiescent galaxies.

The bottom panel shows the constraints on  $w_{\chi}$  for star-forming and quiescent central galaxies. The weights for quiescent centrals are significantly lower than for star-forming centrals, implying a tighter relationship between halo mass and  $c_{\text{gal}}$  for quiescent galaxies. Additionally, the  $w_{\chi}$  values for both subsamples of galaxies show positive slopes, indicating a stronger correlation with  $M_h$  at lower luminosities.

#### 4.3. Satellite fractions and quiescent fractions

We now turn to the constraints on the galaxy-halo connection inferred by the self-calibrated group finder. Figure 9 shows the satellite fractions,  $f_{\text{sat}}$  of star-forming and quiescent galaxies. These values are presented as functions of both  $L_{\text{gal}}$  and  $M_*$ . The shaded regions indicate the 95% confidence intervals on  $f_{\text{sat}}$ . The  $f_{\text{sat}}$  constraints for quiescent galaxies are significantly stronger than for star-forming galaxies. This is due to the constraints on  $B_{\text{sat}}$  presented in the previous subsection. There is essentially no variation of  $B_{\text{sat}}$  for quiescent galaxies fainter than  $\log L_{\text{gal}} = 9.6$ , thus the same subset of quiescent galaxies are labeled as satellites for each model in the posterior.

We also compare our results to other analyses. For  $f_{\text{sat}}(L_{\text{gal}})$ , we compare to the HOD analysis of Zehavi et al. (2011), and the conditional color-magnitude diagram (CCMD) of Xu et al. (2018). Both are based on matching clustering and abundances of galaxies in the MGS. The group catalog results are in good agreement with the Zehavi et al. (2011) results, with the exception of the faintest bin of quiescent galaxies, where the HOD analysis yields  $f_{\text{sat}} \approx 0.9$ . This is the magnitude bin where the group catalog poorly fits the amplitude of the quiescent galaxy clustering. While the prediction of the group catalog is constrained by the actual spatial distribution of SDSS galaxies, in the HOD analysis  $f_{\text{sat}}$  is a completely free parameter, and thus has the freedom to increase the satellite fraction to whatever level is required to match the clustering. However, as is clear from the  $B_{\text{sat}}$  constraints, there simply are not enough quiescent galaxies in the proximity of groups to reach such a high  $f_{\text{sat}}$ . We will discuss possible improvements to the self-calibrated group finder in §5.

Our  $f_{\text{sat}}(L_{\text{gal}})$  results are in good agreement with the CCMD results for quiescent galaxies, but the CCMD satellite fraction of star-forming galaxies is lower than both the group catalog and the HOD results by nearly a factor of two. We will discuss this further in section §4.8, and how it relates to constraints on scatter in the galaxy-halo connection.

The right-hand side of Figure 9 shows the group catalog results for  $f_{\text{sat}}(M_*)$ . As opposed to the results

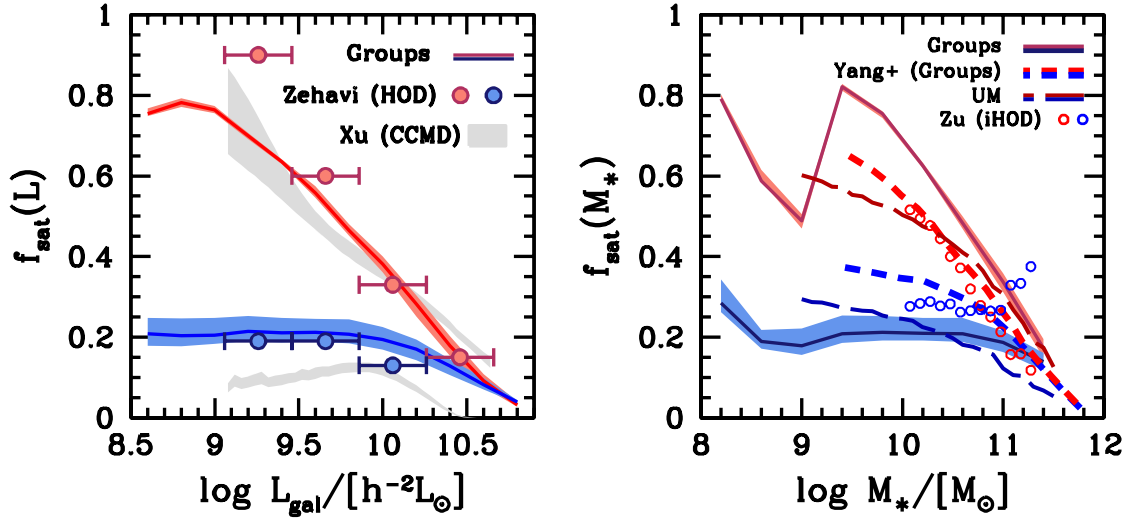


**Figure 9.** *Left Panel:* The satellite fraction,  $f_{\text{sat}}$ , for star-forming and quiescent galaxies, as a function of  $L_{\text{gal}}$ . The blue and red solid curves show the results for the best-fit group catalog, while the shaded regions show the 95% confidence interval on this quantity. The red and blue circles show the results of the HOD fitting of SDSS galaxies from Zehavi et al. (2011). The gray shaded regions show the results for the conditional color magnitude analysis of the SDSS data by Xu et al. (2018), which are not color-coded but are also broken in to star-forming and quiescent samples. *Right Panel:* Same as the opposite panel, but now for stellar mass. Results in this panel are  $1/V_{\text{max}}$ -weighted (see text for details). These results are compared to the Yang et al. (2008a) group catalog, the halo occupation analysis of Zu & Mandelbaum (2016), and the predictions of the UniverseMachine empirical model (Behroozi et al. 2019).

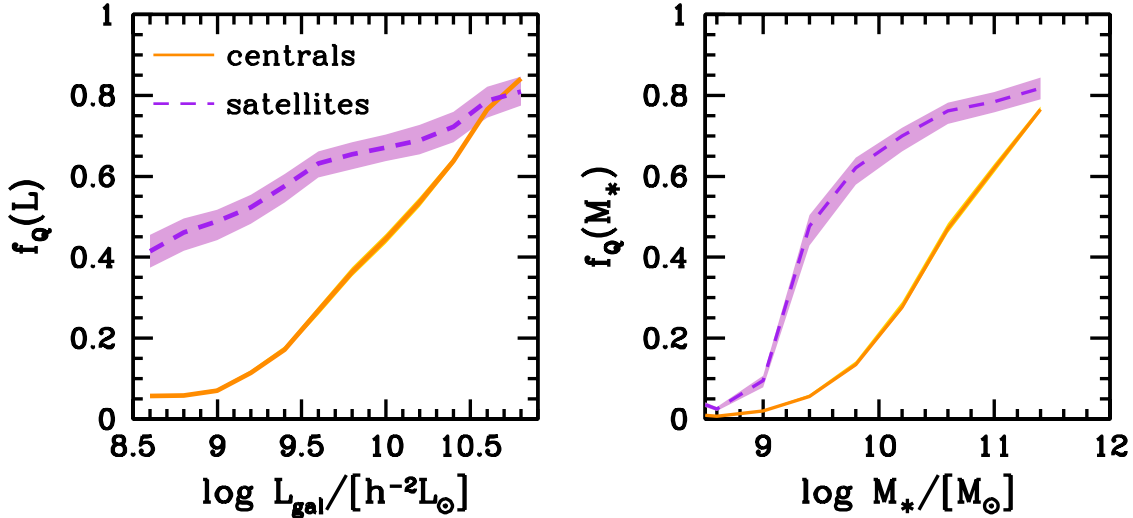


**Figure 10.** *Left Panel:* Quiescent fractions of central and satellite galaxies as a function of  $L_{\text{gal}}$ . The solid and dashed curves show the results for the best-fit group catalog, while the shaded regions show the 95% confidence regions. *Right Panel:* Same as the opposite panel, but now as a function of  $M_*$ . For the  $M_*$  results, all galaxies are  $1/V_{\text{max}}$ -weighted.

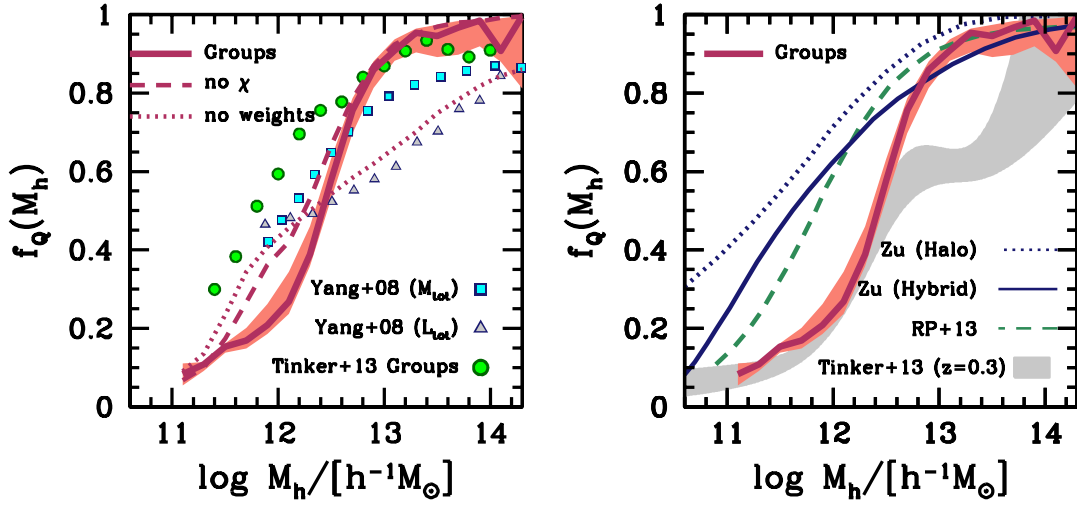


**Figure 11.** *Left Panel:* Quiescent fractions of central and satellite galaxies as a function of  $L_{\text{gal}}$ . The solid curves shows the results for the best-fit group catalog, while the shaded regions show the 95% confidence regions. The dashed curve shows the group results without  $\tilde{L}_{\text{sat}}(\chi)$  data, and the dotted line is the group catalog when removing all weights from  $L_{\text{grp}}$ . The symbols are previous group catalogs, described in the text. *Right Panel:* Same as the opposite panel, but now as a function of  $M_*$ . For the  $M_*$  results, all galaxies are  $1/V_{\text{max}}$ -weighted. The three curves are gray shaded region are halo-occupation based analysis: two parameterizations of quenching from Zu & Mandelbaum (2016), the HOD results of Rodríguez-Puebla et al. (2015), and  $z = 0.3$  halo occupation results from Tinker et al. (2013).



for  $L_{\text{gal}}$ , where each bin in luminosity is effectively a volume-limited sample, each bin in  $M_*$  contains galaxies of varying luminosity, and thus various  $V_{\text{max}}$  values. To account for this, in each bin of  $M_*$ ,  $f_{\text{sat}}$  is calculated as

$$f_{\text{sat}}(M_*) = \frac{\sum_{\text{sats}} 1/V_{\text{max}}}{\sum_{\text{all}} 1/V_{\text{max}}} \quad (9)$$

where the sums in the numerator and the denominator are over all satellites and all galaxies within the stellar mass bin. As with the  $f_{\text{sat}}$  results for luminosity, the constraints for quiescent galaxies are significantly tighter than those for star-forming galaxies. The abrupt change in quiescent  $f_{\text{sat}}$  at  $M_* < 10^9 M_\odot$  is due to finite number statistics: although all results are  $1/V_{\text{max}}$  weighted, the raw number of quiescent galaxies below this stellar mass is only 146.

This figure compares the self-calibrated group catalog results to those of the Yang et al. (2008b). As demonstrated in Paper I, the use of  $B_{\text{sat}} = 10$  for all galaxies yields significant biases in  $f_{\text{sat}}$  which are mirrored in this result:  $f_{\text{sat}}$  for quiescent galaxies is suppressed while the number of star-forming satellites is increased. We also compare to the results of the iHOD analysis of Zu & Mandelbaum (2016). The iHOD analysis is analytic, but the  $f_{\text{sat}}$  results, kindly provided by Y. Zu, are measured from a populated N-body simulation. Thus the results for bright blue galaxies are subject to high shot noise, but are otherwise in agreement with the results from the Yang catalog.

We also compare our results to predictions of the UniverseMachine empirical model of Behroozi et al. (2019), taken from the MOCKUM prepared for testing in Paper I. The satellite fraction for star-forming galaxies is in reasonable agreement with the self-calibrated group results, but  $f_{\text{sat}}$  for quiescent galaxies is somewhat lower.

Figure 10 shows a complementary statistic: the *quiescent fraction*,  $f_q$ , of central and satellite galaxies. As quenching efficiency is higher for satellite galaxies, the expectation is that a higher fraction of satellites will be quiescent than central galaxies (e.g., Weinmann et al. 2006; Wetzel et al. 2012, 2013; Behroozi et al. 2019). The group catalog yields enhanced  $f_q$  values for satellites, when binned both by  $L_{\text{gal}}$  and by  $M_*$ . For  $f_q(L_{\text{gal}})$ , the luminosity at which half of centrals are quiescent is  $\log L_{\text{gal}} = 10.1$ , while for satellites this value is  $\log L_{\text{gal}} = 9.2$ . For  $f_q(M_*)$ , these values for centrals and satellites are  $\log M_* = 10.6$  and 9.4, respectively.

In contrast to the  $f_{\text{sat}}$  results,  $f_q$  for satellites has larger uncertainties than  $f_q$  for centrals, even though the 95% constraints for both are less than a few percent. But  $f_q$  for satellites is determined by the uncertainties in all the probabilities for galaxies to be labeled satellites, and  $B_{\text{sat}}$  for star-forming galaxies has significantly more uncertainty than for quiescent galaxies. For central galaxies, the 95% confidence intervals are barely wider than the curve showing the best-fit model. Al-

though there is some uncertainty on what gets labeled a satellite galaxy, satellites themselves make up  $< 1/3$  of the overall galaxy population, thus the constraints on  $f_q$  for centrals will be stronger by definition.

#### 4.4. Quenching as a function of halo mass

Rather than bin galaxies by their observed properties, it is of interest to investigate how the quiescent fraction of central galaxies depends on *halo mass*. This is one of the main quantities for which previous group catalogs have shown significant biases in Campbell et al. (2015), and one of the goals of the self-calibrated algorithm.

Figure 11 shows  $f_q$  for central galaxies as a function of  $M_h$ . The comparison is split into two panels—in each panel the fiducial group catalog results are the same, but in the left-hand panel we compare to previous group results while on the right we compare our new group results to those constrained by fitting halo occupation models to measurements of clustering and lensing.

First, the left-hand panel of Figure 11 shows how our group results depend on different assumptions in the implementation of the group finder. The thick solid line shows the best-fit group catalog when considering all data. The dashed curve shows the no- $\chi$  group catalog results, meaning all  $w_\chi$  weights are not included in the rank-ordering of the groups. Removing this freedom from the catalog has negligible impact on the results at  $M_h \gtrsim 10^{12.5} h^{-1} M_\odot$ , but it changes the slope of  $f_q$  at lower masses, making the transition from mostly-quiescent central galaxies to mostly-star-forming centrals more gradual. The dotted line is removing all weights of any kind, as well as setting  $B_{\text{sat}} = 10$  for all galaxies. This is effectively the same as the standard halo-base group finder, if the rank-ordering of the groups is based on group luminosity.

The comparison with the gray triangles confirms this, as these data are from the Yang et al. (2008a) group catalog where group ranking is based on  $L_{\text{tot}}$ . The blue squares are the same catalog, but now ranking by total stellar mass of the group instead. As quiescent galaxies at fixed stellar mass have lower luminosities, the blue squares have a much higher  $f_q$  at high halo masses, getting closer to the values found in our self-calibrated group finder that excluded  $L_{\text{sat}}(\chi)$  (dashed line). Last, the green circles show the results of our previous halo-based group finder, with results presented in Tinker et al. (2013). These results differ from the others in that they are performed on volume-limited samples, complete in stellar mass. Here,  $f_q$  is in good agreement with the self-calibrated groups at high halo masses, but once again has a softer transition to groups with majority star-forming central galaxies.

The right-hand panel in Figure 11 compares our group catalog to HOD-based methods. The Zu & Mandelbaum (2016) and Rodríguez-Puebla et al. (2015) analysis are both performed on the SDSS MGS, while the Tinker et al. (2013) results are from analysis of clustering and

lensing within the COSMOS field. [Zu & Mandelbaum \(2016\)](#) present two analyses; one in which quenching is entirely a halo mass-driven process, and another in which quenching is a ‘hybrid’ combination of halo and stellar masses. [Rodríguez-Puebla et al. \(2015\)](#) also parameterize  $f_q$  as a function of  $M_h$ . All three of these models yield quiescent fractions of halos at  $M_h \lesssim 10^{12.5} h^{-1} M_\odot$  significantly higher than that found in the group catalog.

[Tinker et al. \(2013\)](#) implement a non-parametric model for  $f_q(M_h)$  that allows for the non-monotonic behavior seen in the constraints in Figure 11. At the highest mass scales and at  $M_h \lesssim 10^{12.5} h^{-1} M_\odot$ , these results are in good agreement with the self-calibrated groups. But the small area of the COSMOS field—which contributes to the unusual behavior of the  $f_q(M_h)$  constraints is an extra source of uncertainty.

#### 4.5. LHMRs and SHMRs

Figure 12 shows the LHMR and the SHMR predicted by the self-calibrated group finder. We will compare these results to previous results in subsequent figures. For the LHMR, there is a clear change at  $M_h \sim 10^{12} h^{-1} M_\odot$ : not only is this the location of the ‘pivot scale,’ where  $L_{\text{gal}}/M_h$  is maximal, but the LHMRs for star-forming and quiescent galaxies cross. Above this halo mass scale, central star-forming galaxies are more massive than quiescent centrals at the same  $M_h$ . Below this scale, this trend reverses and quiescent galaxies are more massive at fixed  $M_*$ . When binned by  $L_{\text{cen}}$ , as in the comparison to the  $L_{\text{sat}}^q/L_{\text{sat}}^{\text{sf}}$  data in Figure 7, the *halos* of quiescent galaxies are more massive than star-forming galaxies at all  $L_{\text{cen}}$ . As we will see in the following subsection, the scatter of  $\log L_{\text{gal}}$  at fixed  $M_h$  changes significantly across the halo mass spectrum. The larger scatter at low  $M_h$  makes a significant difference in the statistics, depending on whether they are binned by  $M_h$  or by  $L_{\text{cen}}$ .

The impact of scatter on the LHMR is also apparent when comparing the best-fit group catalog to our test catalog where we do not include the  $L_{\text{sat}}(\chi)$  measurements. As discussed in Paper I, without these data, the group catalog cannot differentiate the halos of galaxies at low luminosities. Thus the inferred scatter approaches zero. The dashed lines in Figure 12 show the LHMRs for this catalog. Above the pivot point, there is little difference in the results. At low  $M_h$ , however, the LHMRs for star-forming and quiescent samples come together, and both are offset from the fiducial catalog.

The right-hand side of Figure 12 shows the same results, but for  $M_*$  as opposed to  $L_{\text{gal}}$ . Above the pivot mass, the SHMRs for star-forming and quiescent centrals are closer together—as expected from the fact that quiescent galaxies are fainter at fixed  $M_*$ —but the SHMR for star-forming galaxies is still higher than that of quiescent centrals. The switch below the pivot mass is even more pronounced—at the lowest halo masses

probed, quiescent central galaxies are nearly a dex more massive than star-forming central galaxies at the same  $M_h$ .

#### 4.6. Mass-to-Light ratios

Figure 13 shows the mass-to-light ratios for central galaxies,  $M_h/L_{\text{cen}}$ , broken in to our star-forming and quiescent samples, plotted as a function of  $L_{\text{cen}}$ . We show both the results from our best-fit group catalog as well as the no- $\chi$  catalog. The results of the two catalogs diverge at  $L_{\text{cen}} < 10^{10} h^{-2} L_\odot$ , where the fiducial catalog yields higher  $M_h/L_{\text{cen}}$  ratios. We also note that, at low luminosities, the results of the fiducial catalog show only a small difference in the M/L ratios of star-forming and quiescent samples, analogous to the  $L_{\text{sat}}$  results in Figure 7 discussed earlier.

We compare these results to those of [Lange et al. \(2019\)](#) and the CCMD results of [Xu et al. \(2018\)](#). [Lange et al. \(2019\)](#) use a halo occupation model to fit measurements of satellite kinematics data. Central galaxies are binned by luminosity and separated into red and blue subsamples using the [Zehavi et al. \(2011\)](#) tilted color cut described in §2.1. The [Lange et al. \(2019\)](#) results show the same bimodality in halo masses between star-forming and quiescent samples as seen in the group catalog, although the overall amplitude is shifted down relative to the groups by  $\sim 0.2$  dex. The [Xu et al. \(2018\)](#) results, also separated using the tilted color cut, show color-dependent bimodality in halo masses at  $L_{\text{cen}} \lesssim 10^{10} h^{-2} L_\odot$ . At higher luminosities, the  $M_h/L_{\text{cen}}$  ratios converge. But the consensus from these results—all based on MGS data, binned by  $L_{\text{gal}}$  and separated into star-forming and quiescent samples, but using complementary methods to connect galaxies to halos—is that the  $M_h/L_{\text{cen}}$  for quiescent galaxies is equal to or above that of star-forming centrals.

#### 4.7. Stellar masses of central galaxies

Figure 14, adapted from Figure 8 in [Wechsler & Tinker \(2018\)](#), shows the stellar mass ratio of star-forming and quiescent central galaxies,  $M_{*,q}/M_{*,sf}$ , as a function of  $M_h$ . We show both the fiducial and the no- $\chi$  group results. For both of these catalogs, the  $M_{*,q}/M_{*,sf}$  ratio is below unity at high halo masses and above unity at low halo masses. The two catalogs agree at high halo masses, but at  $M_h \lesssim 10^{13} h^{-1} M_\odot$  the fiducial results are higher than the no- $\chi$  results.

Figure 14 shows the constraints on this quantity from various analyses in the field. The results range from  $M_{*,q}/M_{*,sf}$  being below unity ([Rodríguez-Puebla et al. 2015](#)), above unity ([Moster et al. 2018](#)), and consistent with unity ([Zu & Mandelbaum 2016](#); [Behroozi et al. 2019](#)). The COSMOS analysis of [Tinker et al. \(2013\)](#) is in qualitative agreement with the groups results, in that the mass ratio switches from  $> 1$  to  $< 1$  at roughly the same halo mass scale. The main reason why this is notable is that it is possible to get such a sign change

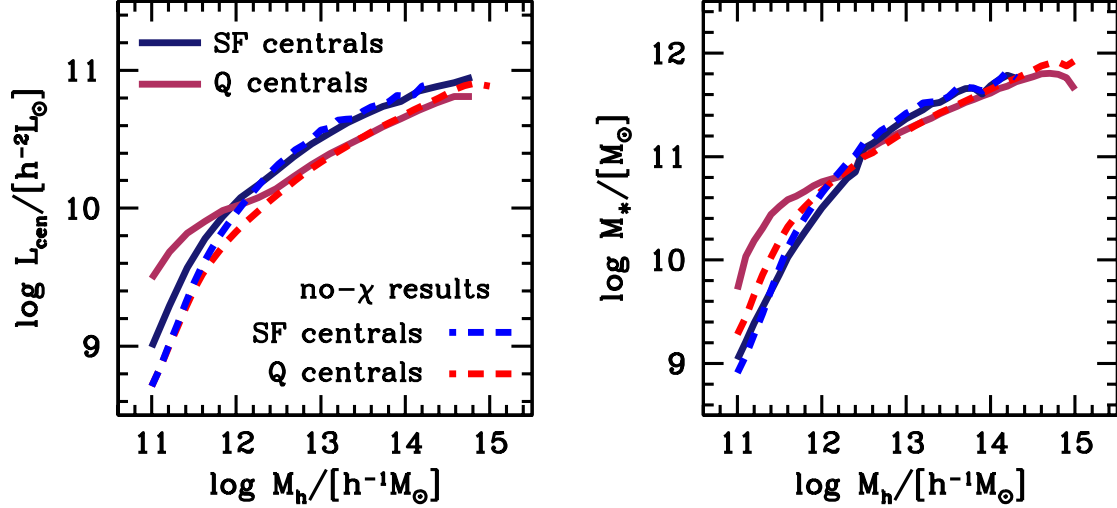


**Figure 12.** *Left Panel:* LHMR for star-forming and quiescent central galaxies from the group catalog. We do not show uncertainties for the quantity because they are nearly the width of the curves for most halo masses. The dashed lines show the results from the group catalog that does not include the  $L_{\text{sat}}(\chi)$  data. Red colors indicate results for quiescent galaxies, while blue colors show results for star-forming galaxies. *Right Panel:* Same as the opposite panel, but now replacing galaxy stellar mass,  $M_*$ , for luminosity.

from a halo occupation analysis, which is not clearly exhibited in the other results.

We further note that the increase in  $M_{*,q}/M_{*,sf}$  at low halo masses is, in part, driven by the choice of  $L_{\text{tot}}$  to rank-order groups as opposed to  $M_{*,\text{tot}}$ . As seen in Figure 12, for the no- $\chi$  results the LHMRs converge at low masses. Thus, the *luminosity* ratio of star-forming and quiescent central galaxies is unity at  $M_h < 10^{12} h^{-1} M_{\odot}$ . The different stellar populations then yield higher stellar masses for quiescent galaxies at fixed  $L_{\text{gal}}$ . However, Figure 12 demonstrates that the fiducial catalog puts higher luminosity quiescent centrals in low-mass halos. Thus, if we use  $M_{*,\text{tot}}$  instead of  $L_{\text{tot}}$ , the mass ratio would still be greater than unity at low  $M_h$ , but possibly with a smaller amplitude.

Figure 15 compares the  $M_{*,q}/M_{*,sf}$  ratio for the fiducial catalog for different stellar mass estimates available for MGS data. For reference, this figure also shows the ratio of luminosities for central galaxies. Here we include our fiducial PCA stellar masses, as well as masses from the MPA-JHU catalog (Brinchmann et al. 2004), Firefly stellar masses (Wilkinson et al. 2017), the stellar masses produced from the *kcorrect* code (Blanton & Roweis 2007), and the M/L-ratio corrected stellar masses of Bell et al. (2003). Compared to the luminosity ratio, all stellar mass ratios show a larger change from low to high halo masses. The specific star formation rate of galaxies increases with decreasing  $M_*$  (e.g., Noeske et al. 2007). Thus, for star-forming galaxies at low luminosities, a larger fraction of the luminosity comes from young stars, even in the *r*-band. For luminous galaxies, the stellar masses of quiescent and star-forming galaxies are closer

together because star-forming galaxies have lower specific star-formation rates. The takeaway from Figure 15, however, is that the shape of  $M_{*,q}/M_{*,sf}$  as a function of  $M_h$  is roughly independent of stellar mass method used.

#### 4.8. Scatter

Figure 16 shows the scatter in  $\log L_{\text{cen}}$  as a function of  $M_h$  for the fiducial group catalog, which we refer to as  $\sigma_{\log L}$ . This quantity is separated into star-forming and quiescent central galaxies. For the best-fit catalog,  $\sigma_{\log L}$  decreases with increasing  $M_h$  for both samples. The uncertainty in the scatter for quiescent centrals is significantly smaller than that of star-forming centrals. For massive halos this is mostly driven by the small numbers of star-forming central galaxies, but it is also driven by the tighter constraints  $w_{\chi}$  for the quiescent sample—as shown in Paper I, the value of  $\sigma_{\log L}$  derived from the group catalog is dependent on the correlation coefficient between  $M_h$  and  $\chi$ . Because of this, the results in Figure 16 should be considered lower limits on the scatter. Due to the differences in  $w_{\chi}$ , however, the scatter for quiescent galaxies is likely to be much closer to the true value than for star-forming centrals.

In this Figure we also compare to the satellite kinematics constraints of Lange et al. (2019) and the CCMD constraints of Xu et al. (2018). Lange et al. (2019) parameterize  $\sigma_{\log L}$  as a linear function of  $\log M_h$ . For the CCMD, the results are more complicated, in that Xu et al. (2018) parameterize the CCMD with ‘pseudo’-blue and -red populations that can overlap, but are then translated into observed color space. Scatter in

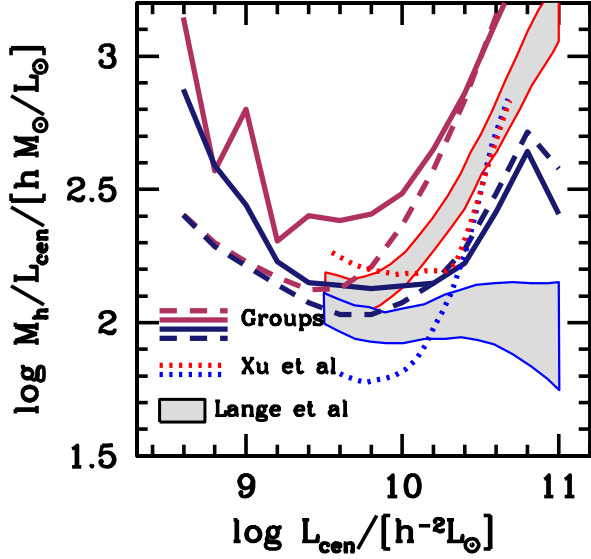


**Figure 13.** Comparing the halo mass-to-light ratio of central galaxies,  $M_h/L_{\text{cen}}$ , of the self-calibrated group catalog to other results. The thick solid curves show the fiducial group catalog, where star-forming and quiescent centrals are indicated by the dark blue and dark red colors. The dashed curves with the same colors indicate the group catalog results that do not include the  $L_{\text{sat}}(\chi)$  data. The shaded region shows the results of the satellite kinematics analysis of Lange et al. (2019). The range indicates the 95% confidence interval from their analysis. The border color corresponds to red and blue galaxy subsamples. The dotted curves show the conditional color-magnitude diagram results of Xu et al. (2018). We have corrected the halo masses of two previous results to account for the difference between  $M_{\text{vir}}$  and  $M_{200b}$ .

the pseudo populations are parameterized in the same log-linear fashion as Lange et al. (2019). In general, all three methods yield consistent constraints, with scatter values centered on  $\sigma_{\log L} \sim 0.2$  dex, and with decreasing scatter as a function of  $M_h$ . The exception is the scatter in luminosity for blue galaxies in the CCMD. As explained in Xu et. al., the smaller scatter is required to match the clustering amplitude of the blue galaxies. This may be related to the lack of blue satellites in the CCMD, seen in Figure 9, which also increase the large-scale bias of the galaxy sample.

Figure 17 shows the scatter in  $\log M_*$  as a function of  $M_h$  for the group catalog, which we refer to as  $\sigma_{\log M_*}$ . Here we show the overall scatter in order to compare with other observational results and theoretical predictions. At large halo masses,  $\sigma_{\log M_*}$  plateaus at  $\sim 0.2$  dex, as compared to 0.15 dex for  $\sigma_{\log L}$ . This reflects the scatter in  $M_*$  at fixed  $L_{\text{gal}}$ . As with the luminosity results,  $\sigma_{\log M_*}$  increases with decreasing  $M_h$ . However, the rise at  $M_h < 10^{13} h^{-1} M_\odot$  is much steeper. This is partly driven by the increased scatter between luminosity and stellar mass for star-forming galaxies, but the

divergence at  $M_h < 10^{11.5} h^{-1} M_\odot$  is possibly affected by incompleteness in the flux-limited catalog. We note that the  $M_*$  results incorporate  $1/V_{\text{max}}$  weighting in all calculations to minimize this effect.

In the upper panel of Figure 17 we compare our results to other observational constraints on  $\sigma_{\log M_*}$ . At  $M_h > 10^{13} h^{-1} M_\odot$ , we compare to estimates from galaxy clusters (To et al. 2020), galaxy groups (Reddick et al. 2013), and the clustering of massive galaxies (Tinker et al. 2017b). These results, as well as other results from the literature (Yang et al. 2009; Leauthaud et al. 2012; Rodríguez-Puebla et al. 2015; Zu & Mandelbaum 2016) converge on a value of  $\sigma_{\log M_*} \sim 0.2$  dex for massive halos.

There are fewer observational constraints at lower halo masses. Cao et al. (2019) used both clustering cross-correlations and line-of-sight velocity distributions to produce two independent constraints that isolate low-mass halos. Additionally, Taylor et al. (2020) used galaxy-galaxy lensing to constrain a lower limit on the scatter in the SHMR. All three of these measurements yield higher values than that seen at high mass scales. The results from the group catalog are in good agreement with all of these observational constraints.

The lower panel in Figure 17, also adapted from Wechsler & Tinker (2018), compares the group results to theoretical predictions. We separate the theoretical predictions into three classes: cosmological hydrodynamical simulations, semi-analytic model of galaxy formation, and empirical models. There is a clear separation between the hydrodynamic and semi-analytic predictions, with semi-analytic models yielding higher scatter values. Both classes of models exhibit an increase<sup>3</sup> in  $\sigma_{\log M_*}$  at low  $M_h$ . The hydrodynamic models show an asymptote at high masses and a steep rise at low masses, while the semi-analytic predictions exhibit a more linear change in scatter. The two empirical model show disparate results, with the EMERGE results consistent with the hydrodynamic simulations and UniverseMachine comparable to the semi-analytic results.

## 5. DISCUSSION

The goals of this paper are two-fold: (1) How to improve the self-calibrated approach to group finding by identifying its strengths and deficiencies in application to real data, and (2) to better understand how the galaxy-halo connection differs for star-forming and quiescent samples of galaxies. We will discuss these goals in turn.

### 5.1. Improving the Self-Calibration Algorithm

The most clear failing of our current implementation of the self-calibrated group finding algorithm is its in-

<sup>3</sup> The downturns in the predictions for both classes of models in the lowest one or two data points is likely a result of resolution limits.



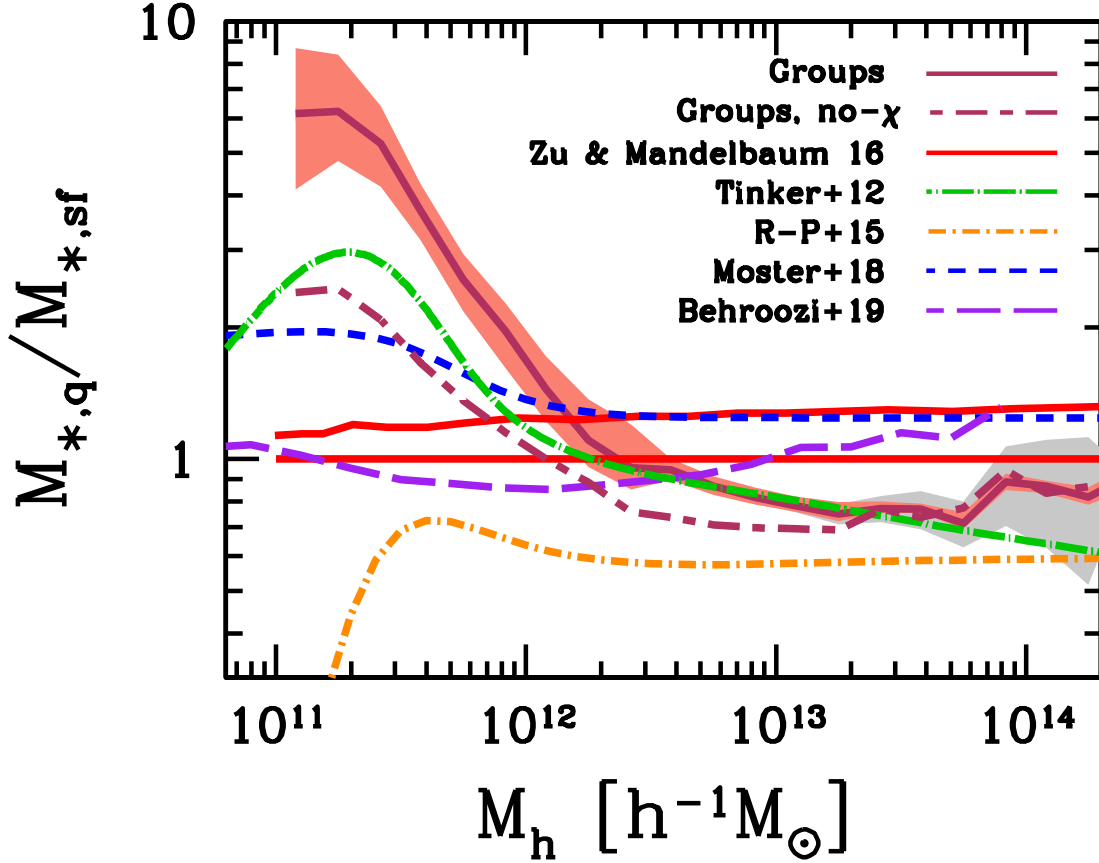


**Figure 14.** The ratio of stellar masses for quiescent and star-forming central galaxies,  $M_{*,q}/M_{*,sf}$ , as a function of  $M_h$ . The solid dark red curve shows the fiducial group catalog results. The red shaded region shows the 95% confidence interval from the MCMC chain, while the gray shaded region shows the  $2\sigma$  Poisson error bars, which only become significant at large halo masses. The dashed curve of the same color shows the group results excluding the  $L_{\text{sat}}(\chi)$  data. The other curves show constraints on this quantity from halo occupation and empirical models.

ability to match the clustering of faint quiescent galaxies. The primary freedom the algorithm has to match clustering is to adjust  $B_{\text{sat}}$  and make more galaxies satellites of a given class. But the parameter constraints in Figure 8—where  $B_{\text{sat},q}$  is at the minimum allowed value for all galaxies fainter than  $L_{\text{gal}} = 10^{9.5} h^{-2} L_{\odot}$  indicates that there simply aren’t enough potential quiescent satellites that exist in the actual MGS galaxy population.

The most likely reason behind this inability is that the model does not incorporate splashback halos in the construction of the clustering predictions. Splashback halos are host halos by our definition—they do not exist within the virial radius of a larger halo—but have passed through a larger halo in the past and thus are subject to significant tidal forces (e.g., Gill et al. 2005). Treating the central galaxies within these halos as ersatz satellite galaxies has been shown to account for the increased quiescent fraction of central galaxies around groups and clusters (Wetzel et al. 2014). Such galaxies increase the overall clustering of the quiescent population because

they reside near large structures and in higher density regions.

It may be that the group finder successfully identifies these galaxies already, but the clustering prediction is constructed by assuming that the halo occupation functions are dependent on  $M_h$  only. The logical step forward is to parametrize the HOD as a function of  $M_h$  and  $\delta_{\text{gal}}$ , where the second parameter is the observed overdensity of galaxies on some scale much larger than the typical halo radius. Theoretical predictions can be made in the same way. Another possible second parameter is the distance to the nearest rich group or cluster, which has been shown to have a strong impact on many halo properties (Salcedo et al. 2018).

The other place where the group catalog’s fit of the data can be improved is with the  $L_{\text{sat}}(\chi)$  measurements. The results of Alpaslan & Tinker (2020) show no correlation between  $c_{\text{gal}}$  and large-scale environment for central galaxies, which is the test for whether secondary halo properties correlate with a given galaxy property at fixed  $M_*$ . However, this test is most efficient at detect-



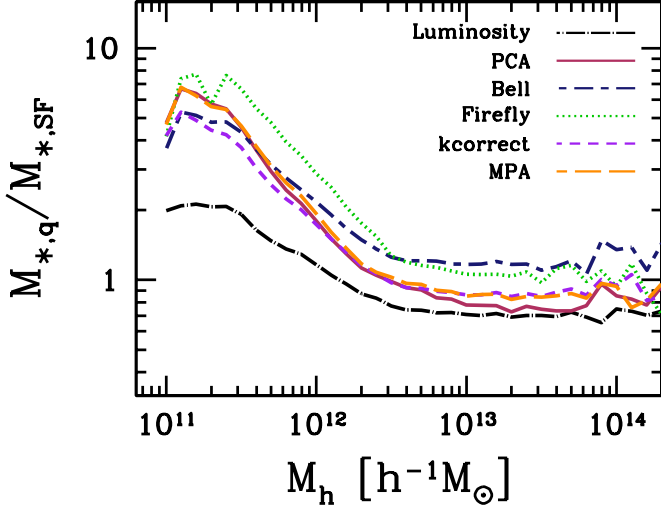


**Figure 15.** The results of Figure 14, but now changing the stellar masses used in the calculation. The PCA results are our fiducial results. These masses and those from the Firefly code use the full spectra of the galaxy to estimate  $M_*$ . The *kcorrect* masses use only the SDSS broadband magnitudes. The MPA masses use a combination of broadband imaging and spectra features. Each show nearly the same trend with  $M_h$ , but with somewhat varying amplitudes. For reference, the ratio of  $L_{\text{cen}}$  for quiescent and star-forming galaxies is also shown.

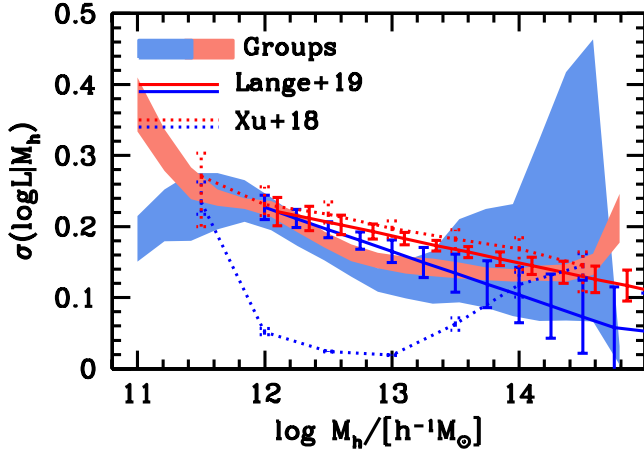


**Figure 16.** Scatter of  $\log L_{\text{cen}}$  as a function of  $M_h$ ,  $\sigma_{\log L}$ . The blue and red shaded contours show the 95% confidence intervals from the group catalog for star-forming and quiescent galaxy samples, respectively. The solid lines are the results from the satellite kinematics analysis of Lange et al. (2019), in which  $\sigma_{\log L}$  is parameterized as a linear function of  $\log M_h$ . Error bars represent 95% confidence intervals on their results. The dotted curves are the results of the CCMD analysis of Xu et al. (2018), which are driven by clustering measurements.

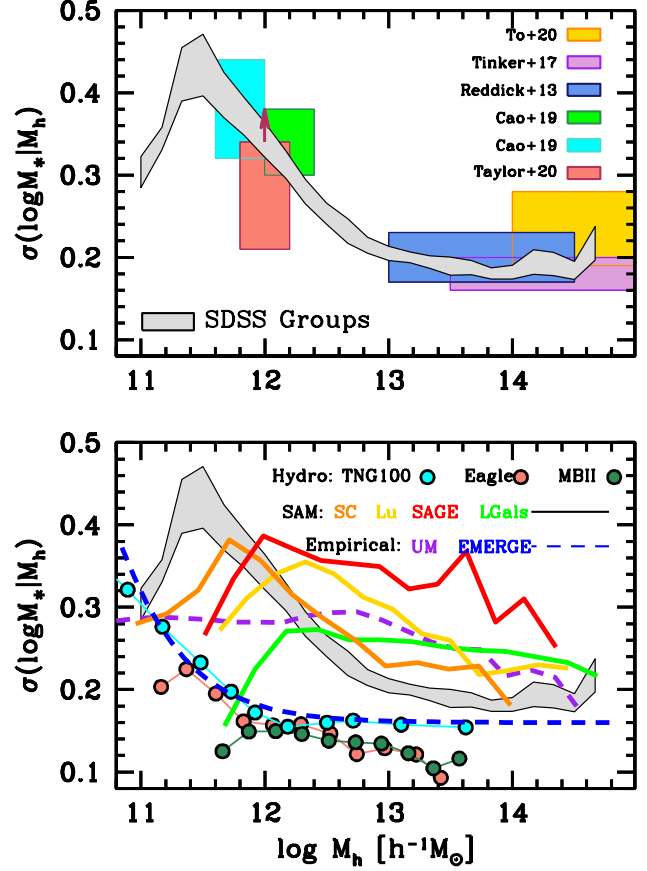


**Figure 17.** *Upper Panel:* A comparison of the scatter in the SHMR between the group catalog and other observational constraints. The gray shaded region shows the 95% confidence interval on  $\sigma_{\log M_*}$ . The observational constraints come from a range of sources. At high halo masses, the results come from clusters (To et al. 2020), clustering (Tinker et al. 2017b), and galaxy groups (Reddick et al. 2013). At lower masses, two independent constraints from Cao et al. (2019), while the results from Taylor et al. (2020) are derived from weak lensing, and represent a lower limit to  $\sigma_{\log M_*}$ . *Lower Panel:* A comparison between group catalog and predictions from numerical simulations. The filled, connected circles show results from hydrodynamic simulations (Pillepich et al. 2018; Matthee et al. 2017; Khandai et al. 2015), semi-analytic models (Somerville et al. 2008; Lu et al. 2014; Henriques et al. 2017; Croton et al. 2016), and empirical models (Behroozi et al. 2019; Moster et al. 2018).

ing strong correlations—if, for example, the influence of halo formation time on  $c_{\text{gal}}$  was subdominant to the that of  $M_h$  but still weakly correlated  $c_{\text{gal}}$ , a more sensitive test would be required.

Toward this end, including secondary halo properties in the model may allow the group catalog to better represent the  $L_{\text{sat}}(\chi)$  data. Additionally, this may allow the group finder to assign not just  $M_h$  to a group, but also

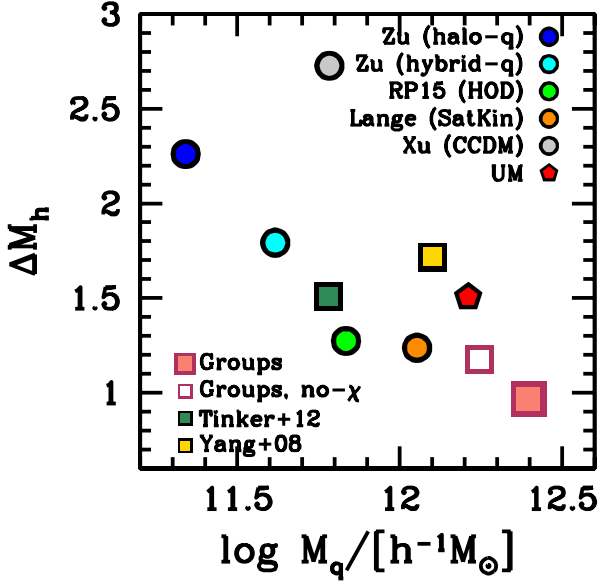


**Figure 18.** Model predictions for the transition between halos that contain star-forming central galaxies to halos with quiescent central galaxies. The  $x$ -axis is the halo mass scale at which 50% of central galaxies are quiescent. The  $y$ -axis is the range in  $\log M_h$  over which halos transition from 20% quiescent to 80% quiescent central galaxies. The circles represent results of studies based on halo occupation analyses. The squares are group catalogs. The pentagon is the prediction of UniverseMachine. The results of our fiducial group catalog are given with the filled red square. For comparison we include the results of the no- $\chi$  catalog as well.

constrain the formation history of the halo that group resides in as well. To accomplish this requires new data to constrain these extra degrees of freedom. [Calderon et al. \(2018\)](#) have shown that marked correlation functions can be more sensitive than other statistical methods of detecting assembly bias is secondary galaxy properties.

In the near term, new data from the DESI-BGS will provide the necessary statistical leverage to expand the freedom in the self-calibration method, as well as providing enhanced constraining power at lower galaxy luminosities where SDSS suffers from low-number statistics. In the longer term, surveys such as WAVES ([Driver et al. 2016](#)) will provide similar space densities but to higher redshift, allowing investigation of the time evolution of the galaxy-halo connection in the group catalog.

### 5.2. The Galaxy-Halo Connection for Star-forming and Quiescent Galaxies

The results of the self-calibrated group finder are different from several previous results in two main ways: the transition in halo mass between star-forming and

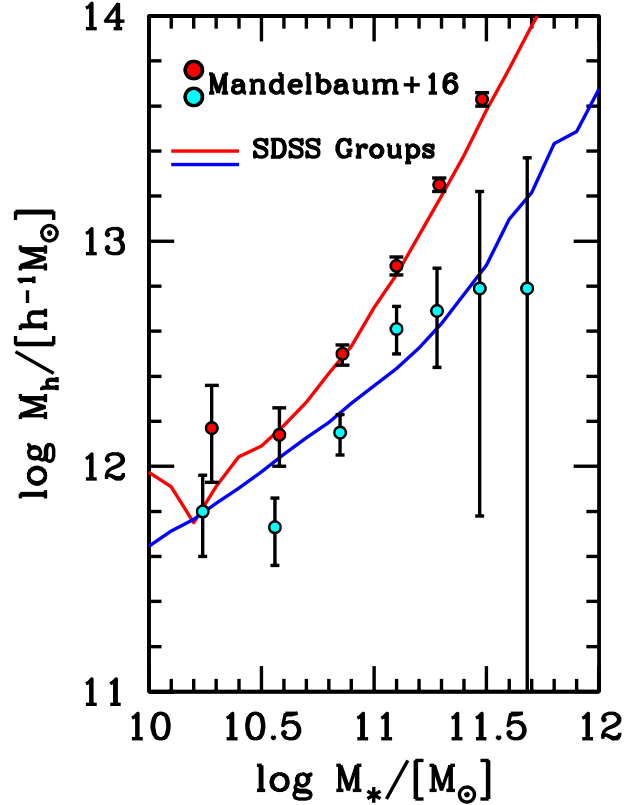


**Figure 19.** Comparing the results of the fiducial group finder to the weak-lensing measurements of halo mass by [Mandelbaum et al. \(2016\)](#). Red curves and symbols indicate results for quiescent central galaxies, while blue curves and symbols show results for star-forming central galaxies.

quiescent central galaxies, and the ratio of the SHMRs between these two populations.

We summarize the results of Figure 11, which is quite busy, with a summary statistic in Figure 18. This statistic is the transition width between star-forming and quiescent halos as a function of the mass scale at which 50% of the halos are quiescent, which we call  $M_{q..}$ . We define the transition width as the difference in  $\log M_h$  between the mass scales at which  $f_q$  is 0.2 and 0.8, which we refer to as  $\Delta M_h$ . For previous studies, values of  $\log M_q$  range between 11.3 to 12.2, while the values of  $\Delta M_h$  range between 1.2 and 2.8<sup>4</sup>. The self-calibrated group finder, however, yields results in this plane that are outside the ranges of all previous results, with the narrowest transition region at the highest halo mass scale. We include in

<sup>4</sup> We note that  $\Delta M_h$  for the CCMD results of [Xu et al. \(2018\)](#) are highly sensitive to the choice of 0.8 as the upper limits on  $f_q$ . The quiescent fraction rises sharply from  $f_q = 0.2$  to  $f_q = 0.7$ , but then flattens out at higher halo masses, yielding the highest value of  $\Delta M_h$ . If we had chosen 0.7 as the upper limit, the [Xu et al. \(2018\)](#) results would have the one of the lowest values.

this figure the group catalog results without the  $L_{\text{sat}}(\chi)$  data for comparison. Although the results have a lower  $M_q$  and wider  $\Delta M_h$ , the changes are minimal and the results of this catalog are still outside the range of other studies.

A primary difference between our analysis and all previous studies is information about the halo masses for low-mass galaxies from  $L_{\text{sat}}$  data. Although weak lensing and satellite kinematics are direct probes of the dark matter gravitational potential around central galaxies, the signal-to-noise of such measurements become weak at  $M_h \lesssim 10^{12} h^{-1} M_\odot$ . The lack of strong information on the halos of central galaxies at these scales is evinced by the results of Figure 18 and also the results Figure 14.

Above these halo mass scales, gravitational lensing offers a independent test of the halo masses assigned in the group catalog. Figure 19 compares the group catalog results to the halo masses measured for SDSS central galaxies in Mandelbaum et al. (2016). To facilitate a proper comparison, the group catalog halo masses are binned in  $M_*$ , using the same MPA stellar masses of the Mandelbaum et. al. analysis. The definition of quiescent in their work is the  $g - r > 0.8$  color cut. This cut was shown to be most similar to our GMM-based  $D_n4000$  cut in Figure 2. The bimodality in weak-lensing inferred halo masses for the different samples is well-matched by the group catalog results. Even though  $L_{\text{sat}}$  is an indirect observable of  $M_h$ , the overall amplitude of the halo mass scales of both blue and red galaxies is reproduced in the group catalog results.

## 6. SUMMARY

In this paper we have applied the novel self-calibrated group finding algorithm, presented in Tinker (2020), to the full flux-limited catalog of the SDSS Main Galaxy Sample. The group finder categorizes each galaxy as central or satellite, and provides an estimate of the halo mass for each group. The upgrade over previous group-finding algorithms is that new finder has extra freedom to assign halos to groups, and this freedom is calibrated by comparing the predictions of the group catalog to measurements of galaxy clustering and measurements of  $L_{\text{sat}}$  around central galaxies.

These changes to the algorithm produce marked changes to the resulting galaxy-halo connection inferred

from group catalogs. A higher fraction of quiescent galaxies are classified as satellites, while a lower fraction of star-forming galaxies are satellites. At high halo masses, star-forming central galaxies are brighter and more massive than quiescent central galaxies in the same halos. But at low halo masses, this ratio inverts, and quiescent central galaxies are several times brighter and more massive than star-forming centrals.

In our catalog, the transition width between star-forming and quiescent halos—in terms of their central galaxies—is outside the range of previous studies, either from group catalogs or halo occupation analyses. Our group catalog finds a narrower transition, in terms of  $\log M_h$ , and a much higher characteristic halo mass scale at which this transition occurs.

The application of the self-calibrated group finder to survey data has highlighted deficiencies in the approach as well. Future implementations will improve by incorporating possible splashback galaxies into the inferred galaxy-halo connection, as well as correlations between secondary halo properties and secondary galaxy properties. New data from the DESI-BGS will expand the statistics that can be used in the self-calibration process, and thus allow more freedom to properly infer the galaxy-halo connection.

The galaxy group catalog, containing central-satellite classification and halo mass estimates for all 550,028 galaxies in the NYU-VAGC, are available publicly<sup>5</sup>.

## ACKNOWLEDGMENTS

JLT gratefully acknowledges the Gauss Centre for Supercomputing e.V. ([www.gauss-centre.eu](http://www.gauss-centre.eu)) and the Partnership for Advanced Supercomputing in Europe (PRACE, [www.prace-ri.eu](http://www.prace-ri.eu)) for funding the MultiDark simulation project by providing computing time on the GCS Supercomputer SuperMUC at Leibniz Supercomputing Centre (LRZ, [www.lrz.de](http://www.lrz.de)). The Bolshoi simulations have been performed within the Bolshoi project of the University of California High-Performance Astro-Computing Center (UC-HiPACC) and were run at the NASA Ames Research Center.

## REFERENCES

- Alpaslan, M., & Tinker, J. L. 2020, MNRAS, doi: [10.1093/mnras/staa1844](https://doi.org/10.1093/mnras/staa1844)
- Baldry, I. K., Balogh, M. L., Bower, R. G., et al. 2006, MNRAS, 373, 469, doi: [10.1111/j.1365-2966.2006.11081.x](https://doi.org/10.1111/j.1365-2966.2006.11081.x)
- Baldry, I. K., Glazebrook, K., Brinkmann, J., et al. 2004, ApJ, 600, 681, doi: [10.1086/380092](https://doi.org/10.1086/380092)
- Balogh, M., Eke, V., Miller, C., et al. 2004, MNRAS, 348, 1355, doi: [10.1111/j.1365-2966.2004.07453.x](https://doi.org/10.1111/j.1365-2966.2004.07453.x)
- Behroozi, P., Wechsler, R. H., Hearin, A. P., & Conroy, C. 2019, MNRAS, 488, 3143, doi: [10.1093/mnras/stz1182](https://doi.org/10.1093/mnras/stz1182)

<sup>5</sup> <https://galaxygroupfinder.net>

- Bell, E. F., McIntosh, D. H., Katz, N., & Weinberg, M. D. 2003, *ApJS*, 149, 289, doi: [10.1086/378847](https://doi.org/10.1086/378847)
- Blanton, M. R., & Berlind, A. A. 2007, *ApJ*, 664, 791, doi: [10.1086/512478](https://doi.org/10.1086/512478)
- Blanton, M. R., & Moustakas, J. 2009, *ARAA*, 47, 159, doi: [10.1146/annurev-astro-082708-101734](https://doi.org/10.1146/annurev-astro-082708-101734)
- Blanton, M. R., & Roweis, S. 2007, *AJ*, 133, 734, doi: [10.1086/510127](https://doi.org/10.1086/510127)
- Blanton, M. R., Hogg, D. W., Bahcall, N. A., et al. 2003, *ApJ*, 594, 186, doi: [10.1086/375528](https://doi.org/10.1086/375528)
- Blanton, M. R., Schlegel, D. J., Strauss, M. A., et al. 2005, *AJ*, 129, 2562, doi: [10.1086/429803](https://doi.org/10.1086/429803)
- Brinchmann, J., Charlot, S., White, S. D. M., et al. 2004, *MNRAS*, 351, 1151, doi: [10.1111/j.1365-2966.2004.07881.x](https://doi.org/10.1111/j.1365-2966.2004.07881.x)
- Calderon, V. F., Berlind, A. A., & Sinha, M. 2018, *MNRAS*, 480, 2031, doi: [10.1093/mnras/sty2000](https://doi.org/10.1093/mnras/sty2000)
- Campbell, D., van den Bosch, F. C., Hearin, A., et al. 2015, *MNRAS*, 452, 444, doi: [10.1093/mnras/stv1091](https://doi.org/10.1093/mnras/stv1091)
- Cao, J.-z., Tinker, J. L., Mao, Y.-Y., & Wechsler, R. H. 2019, *arXiv:1910.03605*, <https://arxiv.org/abs/1910.03605>
- Chen, Y.-M., Kauffmann, G., Tremonti, C. A., et al. 2012, *MNRAS*, 421, 314, doi: [10.1111/j.1365-2966.2011.20306.x](https://doi.org/10.1111/j.1365-2966.2011.20306.x)
- Croton, D. J., Stevens, A. R. H., Tonini, C., et al. 2016, *ApJS*, 222, 22, doi: [10.3847/0067-0049/222/2/22](https://doi.org/10.3847/0067-0049/222/2/22)
- DESI Collaboration, Aghamousa, A., Aguilar, J., et al. 2016, *ArXiv e-prints*, <https://arxiv.org/abs/1611.00036>
- Dey, A., Schlegel, D. J., Lang, D., et al. 2019, *AJ*, 157, 168, doi: [10.3847/1538-3881/ab089d](https://doi.org/10.3847/1538-3881/ab089d)
- Driver, S. P., Davies, L. J., Meyer, M., et al. 2016, *The Universe of Digital Sky Surveys*, 42, 205, doi: [10.1007/978-3-319-19330-4\\_32](https://doi.org/10.1007/978-3-319-19330-4_32)
- Flaugher, B., Diehl, H. T., Honscheid, K., et al. 2015, *AJ*, 150, 150, doi: [10.1088/0004-6256/150/5/150](https://doi.org/10.1088/0004-6256/150/5/150)
- Foreman-Mackey, D., Hogg, D. W., Lang, D., & Goodman, J. 2013, *PASP*, 125, 306, doi: [10.1086/670067](https://doi.org/10.1086/670067)
- Geha, M., Blanton, M. R., Yan, R., & Tinker, J. L. 2012, *ApJ*, 757, 85, doi: [10.1088/0004-637X/757/1/85](https://doi.org/10.1088/0004-637X/757/1/85)
- Gill, S. P. D., Knebe, A., & Gibson, B. K. 2005, *MNRAS*, 356, 1327, doi: [10.1111/j.1365-2966.2004.08562.x](https://doi.org/10.1111/j.1365-2966.2004.08562.x)
- Henriques, B. M. B., White, S. D. M., Thomas, P. A., et al. 2017, *MNRAS*, 469, 2626, doi: [10.1093/mnras/stx1010](https://doi.org/10.1093/mnras/stx1010)
- Kauffmann, G., Heckman, T. M., White, S. D. M., et al. 2003, *MNRAS*, 341, 33, doi: [10.1046/j.1365-8711.2003.06291.x](https://doi.org/10.1046/j.1365-8711.2003.06291.x)
- Khandai, N., Di Matteo, T., Croft, R., et al. 2015, *MNRAS*, 450, 1349, doi: [10.1093/mnras/stv627](https://doi.org/10.1093/mnras/stv627)
- Klypin, A., Yepes, G., Gottlöber, S., Prada, F., & Heß, S. 2016, *MNRAS*, 457, 4340, doi: [10.1093/mnras/stw248](https://doi.org/10.1093/mnras/stw248)
- Lange, J. U., van den Bosch, F. C., Zentner, A. R., Wang, K., & Villarreal, A. S. 2019, *MNRAS*, 487, 3112, doi: [10.1093/mnras/stz1466](https://doi.org/10.1093/mnras/stz1466)
- Leauthaud, A., Tinker, J., Bundy, K., et al. 2012, *ApJ*, 744, 159, doi: [10.1088/0004-637X/744/2/159](https://doi.org/10.1088/0004-637X/744/2/159)
- Li, C., Kauffmann, G., Jing, Y. P., et al. 2006, *MNRAS*, 368, 21, doi: [10.1111/j.1365-2966.2006.10066.x](https://doi.org/10.1111/j.1365-2966.2006.10066.x)
- Lu, Y., Mo, H. J., Lu, Z., Katz, N., & Weinberg, M. D. 2014, *MNRAS*, 443, 1252, doi: [10.1093/mnras/stu1200](https://doi.org/10.1093/mnras/stu1200)
- Mandelbaum, R., Wang, W., Zu, Y., et al. 2016, *MNRAS*, 457, 3200, doi: [10.1093/mnras/stw188](https://doi.org/10.1093/mnras/stw188)
- Matthee, J., Schaye, J., Crain, R. A., et al. 2017, *MNRAS*, 465, 2381, doi: [10.1093/mnras/stw2884](https://doi.org/10.1093/mnras/stw2884)
- Moster, B. P., Naab, T., & White, S. D. M. 2018, *MNRAS*, 477, 1822, doi: [10.1093/mnras/sty655](https://doi.org/10.1093/mnras/sty655)
- Noeske, K. G., Weiner, B. J., Faber, S. M., et al. 2007, *ApJL*, 660, L43, doi: [10.1086/517926](https://doi.org/10.1086/517926)
- Peng, Y.-j., Lilly, S. J., Renzini, A., & Carollo, M. 2012, *ApJ*, 757, 4, doi: [10.1088/0004-637X/757/1/4](https://doi.org/10.1088/0004-637X/757/1/4)
- Pillepich, A., Springel, V., Nelson, D., et al. 2018, *MNRAS*, 473, 4077, doi: [10.1093/mnras/stx2656](https://doi.org/10.1093/mnras/stx2656)
- Reddick, R. M., Wechsler, R. H., Tinker, J. L., & Behroozi, P. S. 2013, *ApJ*, 771, 30, doi: [10.1088/0004-637X/771/1/30](https://doi.org/10.1088/0004-637X/771/1/30)
- Rodríguez-Puebla, A., Avila-Reese, V., Yang, X., et al. 2015, *ApJ*, 799, 130, doi: [10.1088/0004-637X/799/2/130](https://doi.org/10.1088/0004-637X/799/2/130)
- Salcedo, A. N., Maller, A. H., Berlind, A. A., et al. 2018, *MNRAS*, 475, 4411, doi: [10.1093/mnras/sty109](https://doi.org/10.1093/mnras/sty109)
- Somerville, R. S., Hopkins, P. F., Cox, T. J., Robertson, B. E., & Hernquist, L. 2008, *MNRAS*, 1241, doi: [10.1111/j.1365-2966.2008.13805.x](https://doi.org/10.1111/j.1365-2966.2008.13805.x)
- Strauss, M. A., Weinberg, D. H., Lupton, R. H., et al. 2002, *AJ*, 124, 1810, doi: [10.1086/342343](https://doi.org/10.1086/342343)
- Taylor, E. N., Cluver, M. E., Duffy, A., et al. 2020, *arXiv:2006.10040*, *arXiv:2006.10040*, <https://arxiv.org/abs/2006.10040>
- Tinker, J. 2017, in *Galaxy Evolution Across Time*, 46, doi: [10.5281/zenodo.808140](https://doi.org/10.5281/zenodo.808140)
- Tinker, J., Kravtsov, A. V., Klypin, A., et al. 2008, *ApJ*, 688, 709, doi: [10.1086/591439](https://doi.org/10.1086/591439)
- Tinker, J., Wetzel, A., & Conroy, C. 2011, *MNRAS*, submitted, *ArXiv:1107.5046*, <https://arxiv.org/abs/1107.5046>
- Tinker, J. L. 2020, *arXiv e-prints*, *arXiv:2007.12200*, <https://arxiv.org/abs/2007.12200>
- Tinker, J. L., Cao, J., Alpaslan, M., et al. 2019a, *MNRAS*, submitted (*arXiv:1911.04507*), *arXiv:1911.04507*, <https://arxiv.org/abs/1911.04507>
- . 2019b, *arXiv e-prints*, *arXiv:1911.04507*, <https://arxiv.org/abs/1911.04507>

- Tinker, J. L., Hahn, C., Mao, Y.-Y., Wetzel, A. R., & Conroy, C. 2018, *MNRAS*, 477, 935, doi: [10.1093/mnras/sty666](https://doi.org/10.1093/mnras/sty666)
- Tinker, J. L., Leauthaud, A., Bundy, K., et al. 2013, *ApJ*, 778, 93, doi: [10.1088/0004-637X/778/2/93](https://doi.org/10.1088/0004-637X/778/2/93)
- Tinker, J. L., Wetzel, A. R., Conroy, C., & Mao, Y.-Y. 2017a, *MNRAS*, 472, 2504, doi: [10.1093/mnras/stx2066](https://doi.org/10.1093/mnras/stx2066)
- Tinker, J. L., Brownstein, J. R., Guo, H., et al. 2017b, *ApJ*, 839, 121, doi: [10.3847/1538-4357/aa6845](https://doi.org/10.3847/1538-4357/aa6845)
- To, C.-H., Reddick, R. M., Rozo, E., Rykoff, E., & Wechsler, R. H. 2020, *ApJ*, 897, 15, doi: [10.3847/1538-4357/ab9636](https://doi.org/10.3847/1538-4357/ab9636)
- van den Bosch, F. C., & Ogiya, G. 2018, *MNRAS*, 475, 4066, doi: [10.1093/mnras/sty084](https://doi.org/10.1093/mnras/sty084)
- van den Bosch, F. C., Ogiya, G., Hahn, O., & Burkert, A. 2018, *MNRAS*, 474, 3043, doi: [10.1093/mnras/stx2956](https://doi.org/10.1093/mnras/stx2956)
- Wechsler, R. H., & Tinker, J. L. 2018, *ARA&A*, 56, 435, doi: [10.1146/annurev-astro-081817-051756](https://doi.org/10.1146/annurev-astro-081817-051756)
- Weinmann, S. M., van den Bosch, F. C., Yang, X., & Mo, H. J. 2006, *MNRAS*, 366, 2, doi: [10.1111/j.1365-2966.2005.09865.x](https://doi.org/10.1111/j.1365-2966.2005.09865.x)
- Wetzel, A. R., Tinker, J. L., & Conroy, C. 2012, *MNRAS*, 424, 232, doi: [10.1111/j.1365-2966.2012.21188.x](https://doi.org/10.1111/j.1365-2966.2012.21188.x)
- Wetzel, A. R., Tinker, J. L., Conroy, C., & Bosch, F. C. v. d. 2014, *MNRAS*, 439, 2687, doi: [10.1093/mnras/stu122](https://doi.org/10.1093/mnras/stu122)
- Wetzel, A. R., Tinker, J. L., Conroy, C., & van den Bosch, F. C. 2013, *MNRAS*, 432, 336, doi: [10.1093/mnras/stt469](https://doi.org/10.1093/mnras/stt469)
- Wilkinson, D. M., Maraston, C., Goddard, D., Thomas, D., & Parikh, T. 2017, *MNRAS*, 472, 4297, doi: [10.1093/mnras/stx2215](https://doi.org/10.1093/mnras/stx2215)
- Xu, H., Zheng, Z., Guo, H., et al. 2018, *MNRAS*, 481, 5470, doi: [10.1093/mnras/sty2615](https://doi.org/10.1093/mnras/sty2615)
- Yang, X., Mo, H. J., & van den Bosch, F. C. 2008a, *ApJ*, 676, 248, doi: [10.1086/528954](https://doi.org/10.1086/528954)
- . 2008b, *ApJ*, 676, 248, doi: [10.1086/528954](https://doi.org/10.1086/528954)
- . 2009, *ApJ*, 695, 900, doi: [10.1088/0004-637X/695/2/900](https://doi.org/10.1088/0004-637X/695/2/900)
- Yang, X., Mo, H. J., van den Bosch, F. C., & Jing, Y. P. 2005, *MNRAS*, 356, 1293, doi: [10.1111/j.1365-2966.2005.08560.x](https://doi.org/10.1111/j.1365-2966.2005.08560.x)
- York, D. G., et al. 2000, *AJ*, 120, 1579, doi: [10.1086/301513](https://doi.org/10.1086/301513)
- Zehavi, I., Zheng, Z., Weinberg, D. H., et al. 2011, *ApJ*, 736, 59, doi: [10.1088/0004-637X/736/1/59](https://doi.org/10.1088/0004-637X/736/1/59)
- Zhou, Z., Zhou, X., Zou, H., et al. 2018, *PASP*, 130, 085001, doi: [10.1088/1538-3873/aaca7e](https://doi.org/10.1088/1538-3873/aaca7e)
- Zhu, G., Blanton, M. R., Burles, S. M., et al. 2011, *ApJ*, 726, 110, doi: [10.1088/0004-637X/726/2/110](https://doi.org/10.1088/0004-637X/726/2/110)
- Zu, Y., & Mandelbaum, R. 2016, *MNRAS*, 457, 4360, doi: [10.1093/mnras/stw221](https://doi.org/10.1093/mnras/stw221)



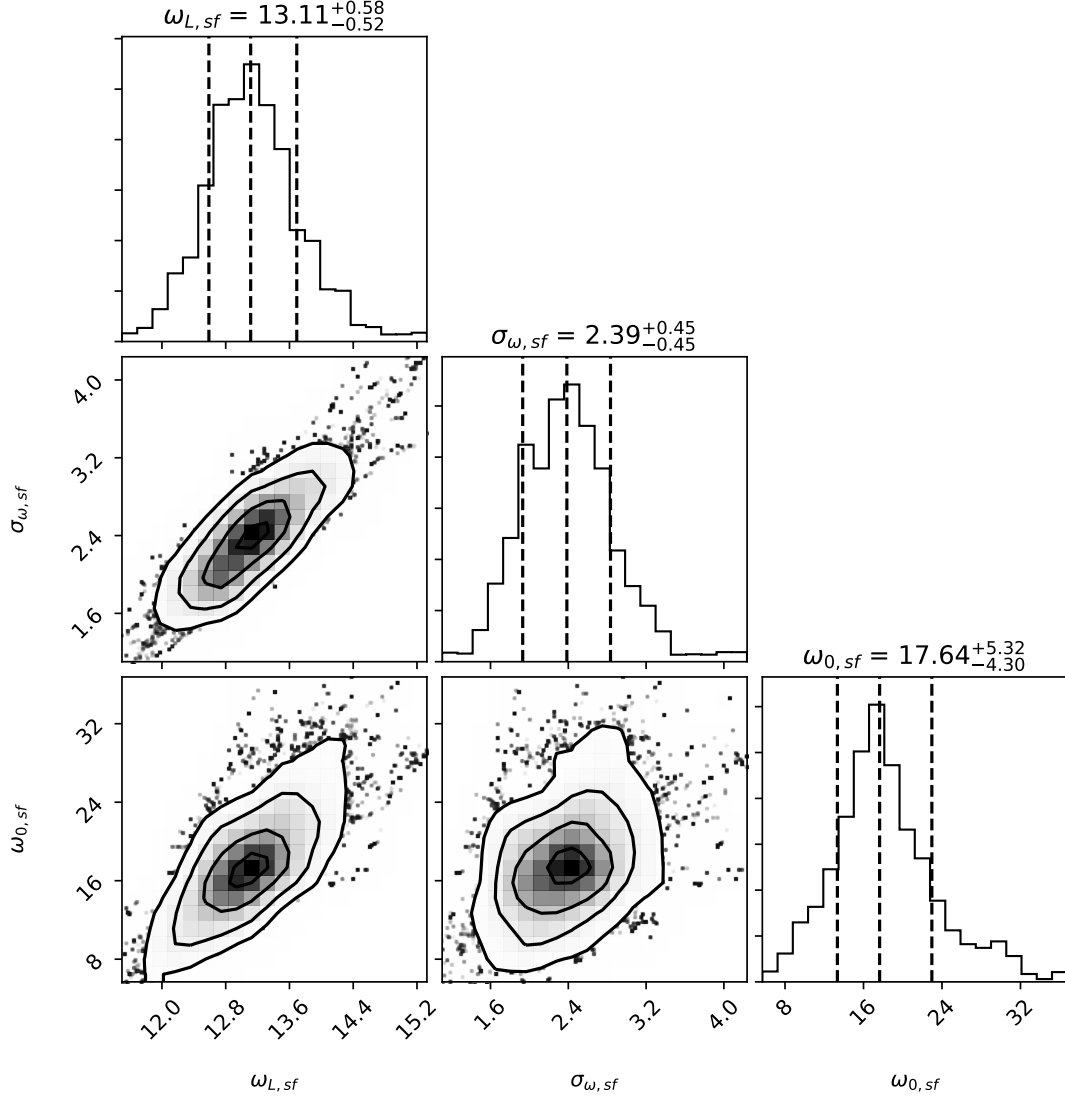


**Figure 20.** Full parameter constraints for the individual parameters in the self-calibration algorithm. This figure shows the parameters of Eq. (5) for star-forming galaxies. Contours show 68%, 95%, and 99% confidence regions. The histograms show the distribution of each parameter, with the median and 68% confidence regions marked with vertical lines.

## APPENDIX

### A. FULL PARAMETER CONSTRAINTS

We use the publicly available python code `emcee` (Foreman-Mackey et al. 2013) to explore the posterior probability distributions of the free parameters in the self-calibration algorithm. The parameters of the best-fit model, as well as 68% confidence intervals, are listed in Table 1. In this appendix, we show corner plots and histograms for all the parameters. The corner plots are broke into four sets, which include the parameters that govern  $w_{\text{cen}}$  for star-forming and quiescent galaxies, satellite threshold parameters  $B_{\text{sat}}$ , and central weights for values of  $\chi$ .

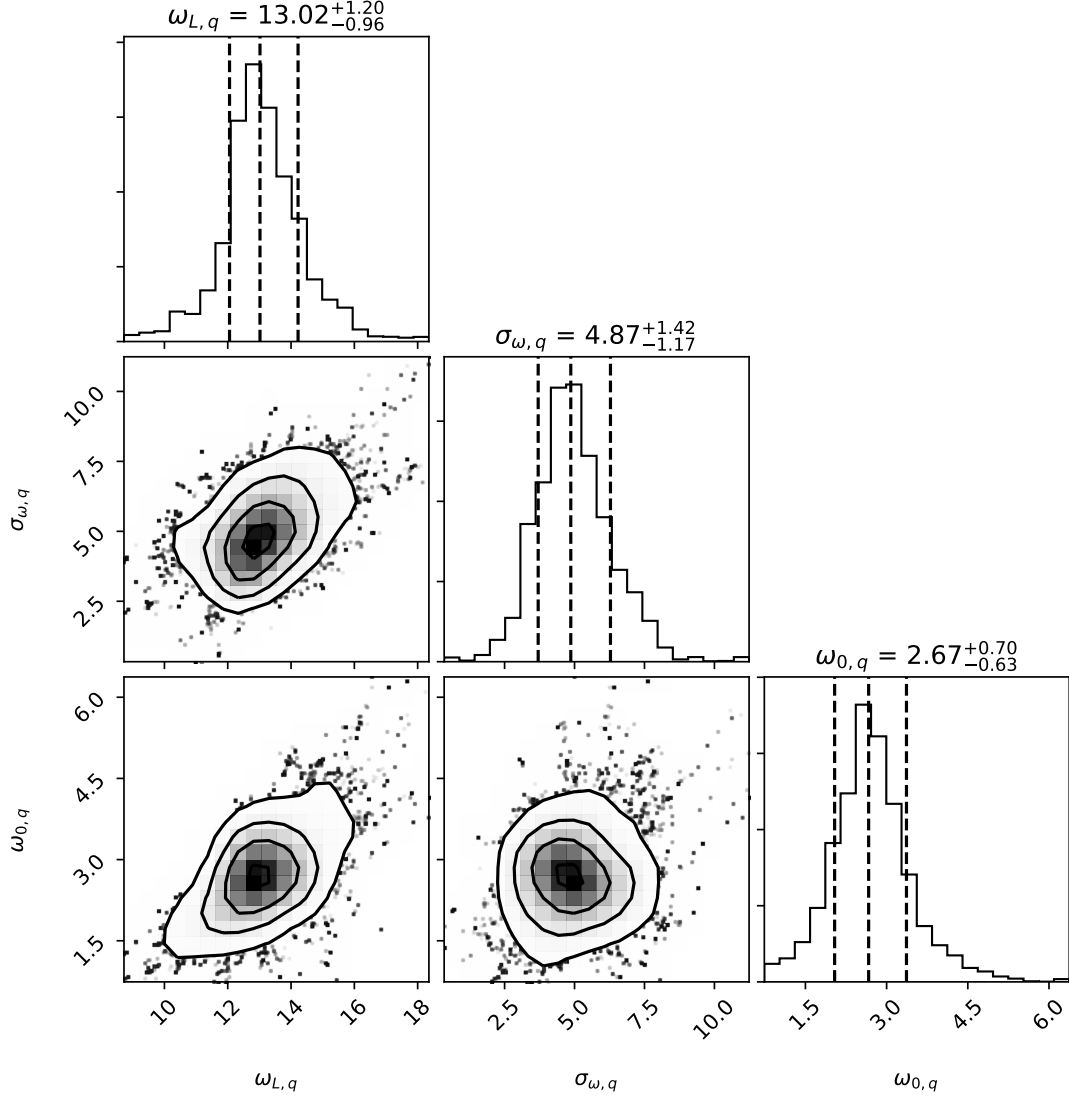


**Figure 21.** Full parameter constraints for the individual parameters in the self-calibration algorithm. This figure shows the parameters of Eq. (5) for quiescent galaxies. Contours show 68%, 95%, and 99% confidence regions. The histograms show the distribution of each parameter, with the median and 68% confidence regions marked with vertical lines.

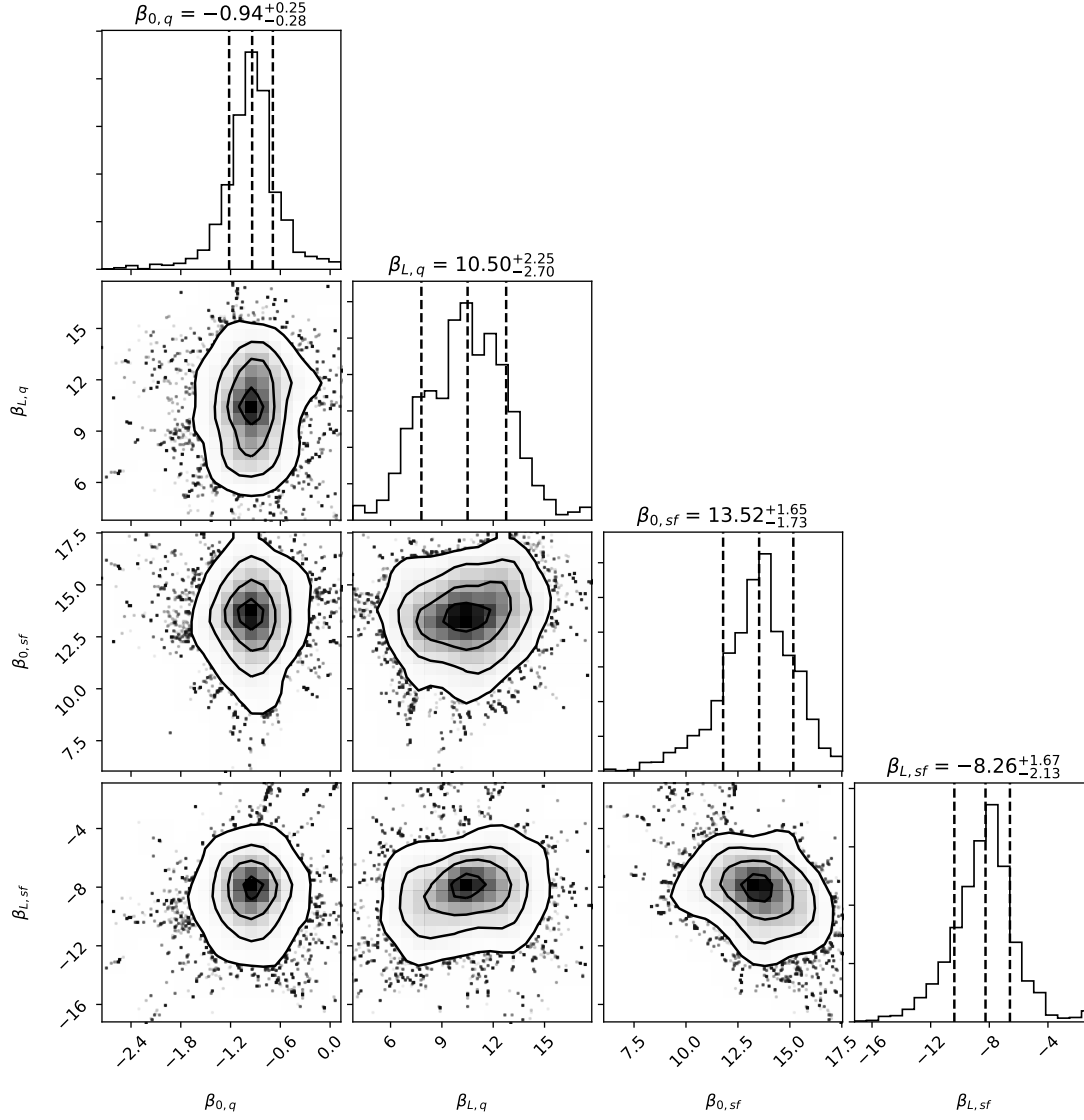


**Figure 22.** Full parameter constraints for the individual parameters in the self-calibration algorithm. This figure shows the parameters of Eq. (4) for both quiescent and star-forming galaxies. Contours show 68%, 95%, and 99% confidence regions. The histograms show the distribution of each parameter, with the median and 68% confidence regions marked with vertical lines.

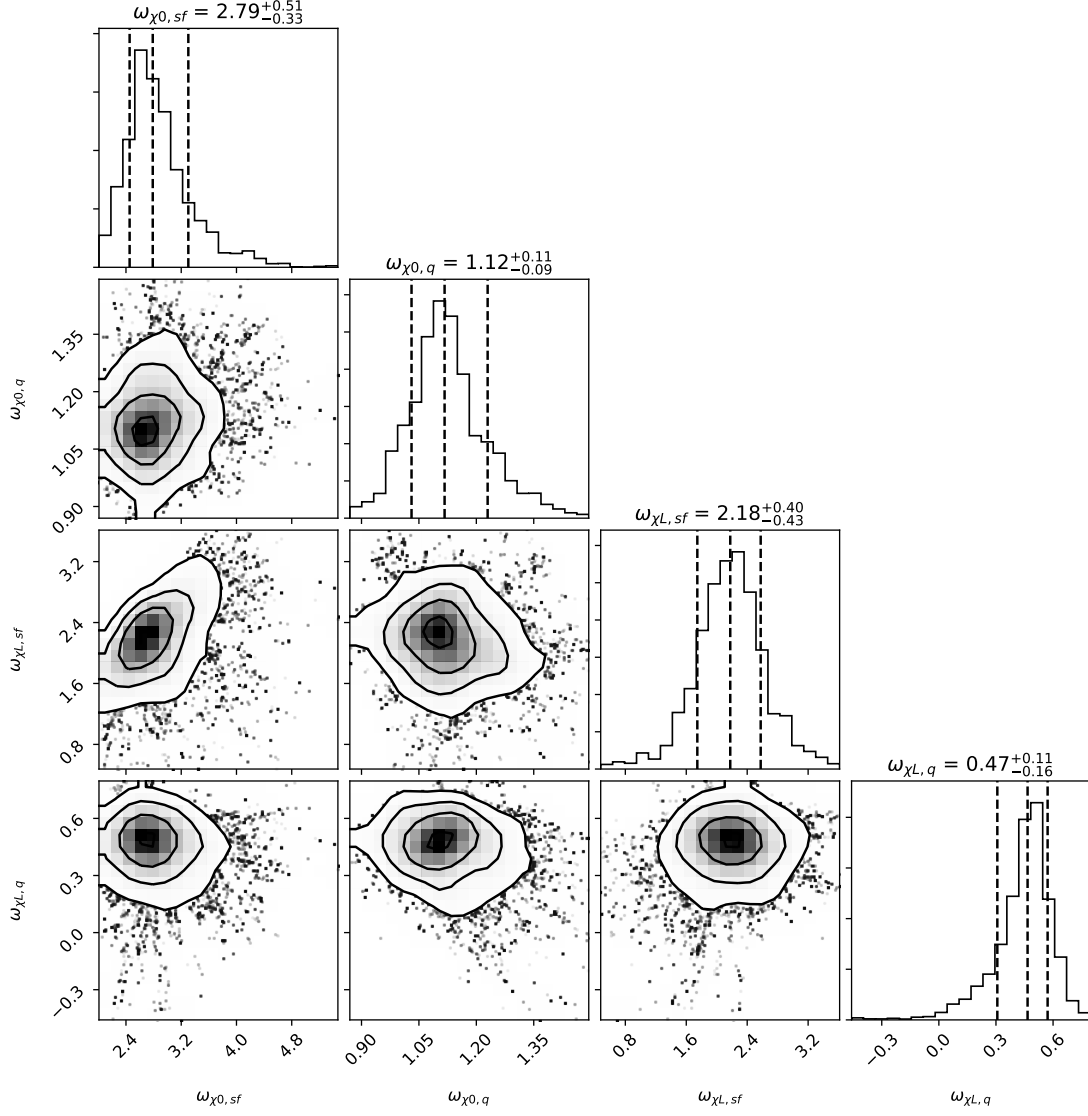


**Figure 23.** Full parameter constraints for the individual parameters in the self-calibration algorithm. This figure shows the parameters of Eq. (6) for quiescent and star-forming galaxies. Contours show 68%, 95%, and 99% confidence regions. The histograms show the distribution of each parameter, with the median and 68% confidence regions marked with vertical lines.